Production of protons, deuterons and tritons in argon-nucleus interactions at 3.2 A GeV

BM@N Collaboration

S. Afanasiev[1], G. Agakishiev[1], A. Aleksandrov[9], E. Aleksandrov[1], I. Aleksandrov[1], P. Alekseev[1,3], K. Alishina[1], V. Astakhov[1], T. Aushev[5], V. Azorskiy[1], V. Babkin[1], N. Balashov[1], R. Barak[1], A. Baranov[8], D. Baranov[1], N. Baranova[8], N. Barbashina[6], S. Bazylev[1], M. Belov[4], D. Blau[3], V. Bocharnikov[7], G. Bogdanova[8], E. Bondar[12], E. Boos[8], E. Bozorov[13], M. Buryakov[1], S. Buzin[1], A. Chebotov[1], D. Chemezov[1], J.H. Chen[11], A. Demanov[1,6], D. Dementev[1], A. Dmitriev[1], J. Drnoyan[1], D. Dryablov[1], B. Dubinchik[1], P. Dulov[1,10], A. Egorov[1], D. Egorov[1], V. Elsha[1], A. Fediunin[1], A. Fedosimova[12], I. Filippov[1], I. Filozova[1], D. Finogeev[2], I. Gabdrakhmanov[1], O. Gavrischuk[1], K. Gertsenberger[1], O. Golosov[6], V. Golovatyuk[1], P. Grigoriev[1], M. Golubeva[2], F. Guber[2], S. Ibraimova[12], D. Idrisov[2], T. Idrissova[12], A. Ivashkin[2], A. Izvestnyy[2], V. Kabadzhov[10], A. Kakhorova[13], Sh. Kanokova[13], M. Kapishin[1], I. Kapitonov[1], V. Karjavin[1], D. Karmanov[8], N. Karpushkin[1,2], R. Kattabekov[1], V. Kekelidze[1], S. Khabarov[1], P. Kharlamov[1,8], G. Khudaiberdyev[13], A. Khvorostukhin[1], V. Kireyeu[1], Yu. Kiryushin[1], P. Klimai[2,5], V. Kolesnikov[1], A. Kolozhvari[1], Yu. Kopylov[1], M. Korolev[8], L. Kovachev[1,14], I. Kovalev[8], Yu. Kovalev[1], V. Kozlov[4], I. Kruglova[1], S. Kuklin[1], E. Kulish[1], A. Kurganov[8], V. Kutergina[1], A. Kuznetsov[1], E. Ladygin[1], D. Lanskoy[8], N. Lashmanov[1], I. Lebedev[12], V. Lenivenko[1], R. Lednicky[1], V. Leontiev[1,8], E. Litvinenko[1], D. Lyapin[2], Y.G. Ma[11], A. Makankin[1], A. Makhnev[2], A. Malakhov[1], M. Mamaev[1,6], A. Martemianov[3], M. Merkin[8], S. Merts[1], S. Morozov[1,2], Yu. Murin[1], K. Musaev[13], G. Musulmanbekov[1], D. Myktybekov[12], R. Nagdasev[1], S. Nemnyugin[9], D. Nikitin[1], R. Nizamov[9], S. Novozhilov[1], A. Olimov[13],Kh. Olimov[13], K. Olimov[13], V. Palichik[1], P. Parfenov[1,6], I. Pelevanyuk[1], D. Peresunko[3], S. Piyadin[1], M. Platonova[8], V. Plotnikov[1], D. Podgainy[1], I. Pshenichnov[2], N. Pukhaeva[1], F. Ratnikov[7], S. Reshetova[1], V. Rogov[1], I. Romanov[1], I. Rufanov[1], P. Rukoyatkin[1], M. Rumyantsev[1], T. Rybakov[3], D. Sakulin[1], S. Savenkov[2], D. Serebryakov[2], A. Shabanov[2], S. Sergeev[1], A. Serikkanov[12], A. Sheremetev[1], A. Sheremeteva[1], A. Shchipunov[1], M. Shitenkov[1],

M. Shodmonov[13], M. Shopova[10], A. Shutov[1], V. Shutov[1], I. Slepnev[1], V. Slepnev[1], I. Slepov[1], A. Smirnov[1], A. Solomin[8], A. Sorin[1], V. Spaskov[1], A. Stavinskiy[1,3], V. Stekhanov[3], Yu. Stepanenko[1], E. Streletskaya[1], O. Streltsova[1], M. Strikhanov[6], E. Sukhov[1], D. Suvarieva[1,10], A. Svetlichnyy[2], G. Taer[3], A. Taranenko[1,6], N. Tarasov[1], O. Tarasov[1], P. Teremkov[4], A. Terletsky[1], O. Teryaev[1], V. Tcholakov[10], V. Tikhomirov[1], A. Timoshenko[1], O. Tojiboev[13], N. Topilin[1], T. Tretyakova[8], V. Troshin[1,6], A. Truttse[6], I. Tserruya[15], V. Tskhay[4], I. Tyapkin[1], V. Ustinov[1], V. Vasendina[1], V. Velichkov[1], V. Volkov[2], A. Voronin[8], A. Voronin[1], N. Voytishin[1], B. Yuldashev[13], V. Yurevich[1], N. Zamiatin[1], M. Zavertyaev[4], S. Zhang[11], I. Zhavoronkova[1,6], N. Zhigareva[3], A. Zinchenko[1], R. Zinchenko[1], A. Zubankov[2], E. Zubarev[1], M. Zuev[1]

1 Joint Institute for Nuclear Research (JINR), Dubna, Russia
2 Institute for Nuclear Research of the RAS (INR RAS), Moscow, Russia
3 Kurchatov Institute, NRC, Moscow, Russia
4 Lebedev Physical Institute of the Russian Academy of Sciences (LPI RAS), Moscow, Russia
5 Moscow Institute of Physics and Technology (MIPT), Moscow, Russia
6 National Research Nuclear University MEPhI, Moscow, Russia
7 National Research University Higher School of Economics (HSE University), Moscow, Russia
8 Skobeltsyn Institute of Nuclear Physics, Moscow State University (SINP MSU), Moscow, Russia
9 St Petersburg University (SPbU), St Petersburg, Russia
10 Plovdiv University "Paisii Hilendarski", Plovdiv, Bulgaria
11 Key Laboratory of Nuclear Physics and Ion-Beam Application (MOE), Institute of Modern Physics, Fudan University, Shanghai, China
12 Institute of Physics and Technology, Satbayev University, Almaty, Kazakhstan
13 Physical-Technical Institute of Uzbekistan Academy of Sciences (PhTI of UzAS), Tashkent, Uzbekistan
14 Institute of Mechanics at the Bulgarian Academy of Sciences (IMech-BAS), Sofia, Bulgaria
15 Weizmann Institute of Science, Rehovot, Israel

Abstract

Results of the BM@N experiment at the Nuclotron/NICA complex are presented on proton, deuteron and triton production in interactions of an argon beam of 3.2 A GeV with fixed targets of C, Al, Cu, Sn and Pb. Transverse mass spectra, rapidity distributions and multiplicities of protons, deuterons and tritons are measured. The results are treated within a coalescence approach and compared with predictions of theoretical models and with other measurements.

1 Introduction

BM@N (Baryonic Matter at Nuclotron) is the first operational experiment at the Nuclotron/NICA accelerator complex. The Nuclotron provides beams of a variety of particles, from protons up to gold ions, with kinetic energy in the range from 1 to 6 A GeV for light ions with Z/A ratio of ~ 0.5 and up to 4.5 A GeV for heavy ions with Z/A ratio of ~ 0.4. At these energies, the nucleon density in the fireball created in heavy-ion beam collisions with fixed targets is 3–4 times higher than the nuclear saturation density [1], thus allowing one to study heavy-ion interactions in the high-density baryonic matter regime [2–5].

During the commissioning phase, BM@N, in a configuration with limited phase-space coverage, collected its first data with beams of carbon, argon and krypton ions [6,7]. In the first physics publication, BM@N reported studies of π^+ and K^+ production in argon-nucleus interactions [8]. This paper presents results on proton, deuteron and triton production in 3.2 A GeV argon-nucleus interactions.

At the Nuclotron energies, baryon transfer over finite rapidity distances (baryon stopping [9]) plays an important role [10]– [12]. The baryon density achieved in high-energy nuclear collisions is a crucial quantity that governs the reaction dynamics and the overall system evolution, including eventual phase transitions. The baryon rapidity distributions in heavy ion collisions for different combinations of projectile and target as well as at different impact parameters provide essential constraints on the dynamical scenarios of baryon stopping. The BM@N experimental setup allows for the measurement of the distribution of protons and light nuclei (d, t) over the rapidity interval [1.0–2.2]. This rapidity range is wide enough to include not only the midrapidity (y_{CM} = 1.08) but also the beam rapidity region (y_{beam} = 2.16), in contrast to the collider experiments, where the acceptance is usually focused only in the mid-rapidity region. Together with a sufficient transverse momentum (p_T) coverage for nuclear clusters, it is possible at BM@N to better determine the shape of the rapidity density distribution and derive information about rapidity and energy loss in the reaction.

Nuclear cluster production allows one to estimate the nucleon phase-space density attained in the reaction [13]. It governs the overall evolution of the reaction process and may provide information about freeze-out conditions and entropy production in relativistic nucleus-nucleus interactions. The nucleon phase space density can be obtained from the ratio of deuteron and proton abundances. One of the goals of this work is to study the particle phase-space density evolution in Ar+A collisions for different projectile-target combinations and as a function of collision centrality.

In collisions of heavy nuclei at relativistic energies, a significant fraction of the initial kinetic energy transforms into particle production and thermal excitation of matter. Various dynamical models, including those based on hydrodynamics, have demonstrated that the entropy per baryon S/A created during the initial interaction stage remains constant during the subsequent evolution of the system [16, 17]. Thus, data about entropy production provides insights not only into the nucleon phase-space density at the final moments of the reaction (freeze-out) but also about the medium properties during the hot and compressed stage. It is also the aim of this work to investigate the entropy evolution in the reaction zone with system size in argon-nucleus collisions and compare BM@N results with other existing experimental data.

The binding energies of deuterons and tritons are small compared to the freeze-out temperatures, which are on the order of 100 MeV. These light clusters are therefore not expected to survive through the high density stages of the collision. The deuterons and tritons observed in the experiment form and emit at the end of the freeze-out process, carrying information about this late stage of the collision.

Light cluster production in low-energy heavy-ion collisions is well described in a simple coalescence model [18–21] through the distributions of their constituents (protons and neutrons) and a coalescence parameter B_A related to the cluster size A. To describe heavy-ion collisions at high energies, the simple coalescence model is modified to account for the nucleon phase space distributions at freeze-out as well as the strength of momentum-space correlations induced by collective flow [22]. In central heavy-ion collisions, the pressure gradient in the system generates strong transverse radial flow. Therefore nucleon clusters inside a collective velocity field acquire additional momentum proportional to the cluster's mass.

The paper is organized as follows: section 2 describes the experimental setup, section 3 details the event reconstruction, and section 4 discusses the evaluation of proton, deuteron, and triton reconstruction efficiency. Section 5 explains the methodology for the definition of centrality classes. Section 6 addresses the evaluation of the cross sections, multiplicities and systematic uncertainties. Transverse mass distributions and rapidity spectra of protons, deuterons and tritons are given in section 7. The BM@N results are compared with predictions of the DCM-SMM [23, 24] and PHQMD [25] models. Ratios of the transverse momentum distributions of deuterons and tritons to protons are treated within a coalescence approach in section 8. The results are compared with other experimental data on nucleus-nucleus interactions. Results on baryon rapidity loss in argon-nucleus interactions are presented in section 9. The compound ratios of yields of protons and tritons to deuterons are presented in section 10. Finally, a summary is given in section 11.

2 Experimental setup

The BM@N detector is a forward spectrometer covering the pseudorapidity range $1.6 \leq \eta \leq 4.4$. A schematic view of the BM@N setup in the argon-beam run is shown in figure 1. More details of all components of the setup can be found in [26, 27]. The spectrometer includes a central tracking system consisting of 3 planes of forward silicon-strip detectors (ST) and 6 planes of detectors based on gas electron multipliers (GEM) [28]. The central tracking system is located downstream of the target region inside of a dipole magnet with a bending power of about 2.1 Tm and with a gap of 1.05 m between the poles. In the measurements reported here, the central tracker covered only the upper half of the magnet acceptance.

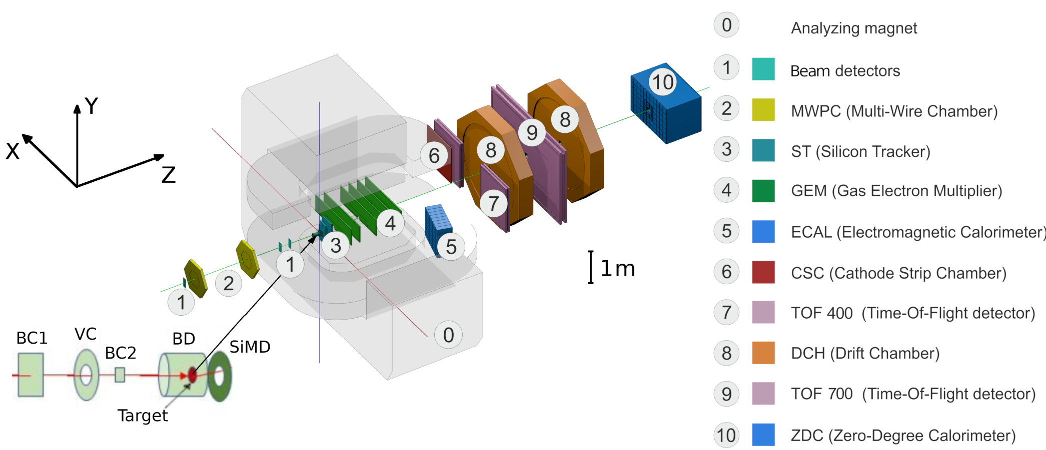

Figure 1. Schematic view of the BM@N setup in the argon beam run.

Two sets of drift chambers (DCH), a cathode strip chamber (CSC), two sets of time-of-flight detectors (ToF), and a zero-degree calorimeter (ZDC) are located downstream of the dipole magnet. The tracking system measures the momentum of charged particles with a relative uncertainty that varies from 2.5% at a momentum of 0.5 GeV/c to 2% from 1 to 2 GeV/c and rises linearly to 6.5% at 5 GeV/c. The time resolutions of the ToF-400 [29] and ToF-700 [30] systems are 84 ps and 115 ps, respectively [31].

Two beam counters (BC1, BC2), a veto counter (VC), a barrel detector (BD), and a silicon multiplicity detector (SiMD) are used for event triggering and for measurement of the incoming beam ions. The BC2 counter also provides the start time T0 for the time-of-flight measurement. The BD detector consists of 40 azimuthal scintillating strips arranged around the target, and the SiMD detector consists of 60 azimuthal silicon segments situated behind the target.

Data were collected with an argon beam intensity of a few 10^5 ions per spill and a spill duration of 2–2.5 sec. The kinetic energy of the beam was 3.2 A GeV with a spread of about 1%. A set of solid targets of various materials (C, Al, Cu, Sn and Pb) with an interaction length of 3% was used. The experimental data correspond to a total integrated luminosity of 7.8 $\mu\mathrm{b}^{-1}$ collected with the different targets: 2.1 $\mu\mathrm{b}^{-1}$ (C), 2.3 $\mu\mathrm{b}^{-1}$ (Al), 1.8 $\mu\mathrm{b}^{-1}$ (Cu), 1.1 $\mu\mathrm{b}^{-1}$ (Sn), 0.5 $\mu\mathrm{b}^{-1}$ (Pb). A total of 16.3 M argon-nucleus collisions at 3.2 A GeV were reconstructed.

To count the number of beam ions that passed through the target, a logical beam trigger BT = BC1$\wedge\overline{\mathrm{VC}}\wedge$BC2 was used. The following logic conditions were applied to generate the trigger signal: 1) BT$\wedge$(BD$\geq 3,4$); 2) BT$\wedge$(SiMD$\geq 3,4$); 3) BT$\wedge$(BD$\geq$ 2)$\wedge$(SiMD$\geq$ 3). The trigger conditions were varied to find the optimal ratio between the event rate and the trigger efficiency for each target. Trigger condition 1 was applied for 60% of the data collected with the carbon target. This trigger fraction was continuously reduced with the atomic weight of the target down to 26% for the Pb target. The fraction of data collected with trigger condition 2 was increased from 6% for the carbon target up to 34% for the Pb target. The rest of the data were collected with trigger condition 3.

3 Event reconstruction

Track reconstruction in the central tracker is based on a "cellular automaton" approach [32] implementing a constrained combinatorial search of track candidates with their subsequent fitting by a Kalman filter to determine the track parameters. These tracks are used to reconstruct primary and secondary vertices as well as global tracks by extrapolation and matching to hits in the downstream detectors (CSC, DCH and ToF).

The primary collision vertex position (PV) is measured with a resolution of 2.4 mm in the X–Y plane perpendicular to the beam direction and 3 mm in the beam direction.

Charged particles (protons, deuterons and tritons) are identified using the time of flight Δt measured between T0 and the ToF detectors, the length of the trajectory Δl, and the momentum p reconstructed in the central tracker. Then the squared mass M^2 of the particle is calculated by the formula: $M^2 = p^2((\Delta tc/\Delta l)^2 - 1)$, where c is the speed of light.

The following criteria are required for selecting proton, deuteron and triton candidates:

- Each track has at least 4 hits in the GEM detectors (6 detectors in total) [28]. Hits in the forward silicon detectors are used to reconstruct the track, but no requirements are applied to the number of hits.

- Tracks originate from the primary vertex. The deviation of the reconstructed vertex Z_{ver} from the nominal target position along the beam direction Z_0 is limited to -3.4 cm $< Z_{\text{ver}} - Z_0 <$ 1.7 cm. The upper limit corresponds to $\sim 5.7\sigma$ of the Z_{ver} spread and cuts off interactions with the trigger detector located 3 cm behind the target. The beam interaction rate with the trigger detector is well below 1% and was not simulated since it does not affect the precision in Monte Carlo simulation.

- Distance from the track to the primary vertex in the X–Y plane at Z_{ver}(DCA) is required to be less than 1 cm, which corresponds to 4σ of the vertex residual distribution in the X–Y plane.

- Momentum range of positively charged particles is limited by the acceptance of the ToF-400 and ToF-700 detectors to $p > 0.5$ GeV/c and $p > 0.7$ GeV/c, respectively.

- Distance of extrapolated tracks to the CSC (DCH) hits as well as to the ToF-400 (ToF-700) hits should be within $\pm 2.5\sigma$ of the momentum dependent hit-track residual distributions.

The mass squared (M^2) spectra of positively charged particles produced in interactions of the 3.2 A GeV argon beam with various targets are shown in figures 2a and 2b for ToF-400 and ToF-700 data, respectively. Particles that satisfy the above selection criteria contribute to the M^2 spectra. The proton, deuteron and triton signals are extracted in M^2 windows, which depend on rapidity, and at the maximal rapidity extend from 0.4–1.7 (GeV/c^2)^2, 2.3–5.0 (GeV/c^2)^2 and 6.6–10.0 (GeV/c^2)^2, respectively. The signals of protons, deuterons and tritons and their statistical errors are calculated according to the formulae: $sig = hist - bg$, where $hist$ denotes the histogram integral yield within the selected M^2-window, and bg is the background.

(a) (b)

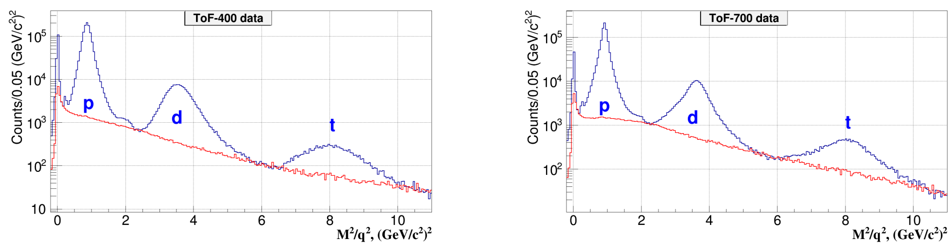

Figure 2. M^2/q^2 spectra of positively charged particles produced in argon-nucleus interactions and measured in the ToF-400 (a) and ToF-700 (b) detectors. Peaks of protons, deuterons and tritons with the charge $q = 1$ are indicated; the small peaks of He fragments with $q = 2$ either overlap with the deuteron one (He^4) or show up at $M^2/q^2 \sim 2$ (GeV/c^2)^2(He^3). The red histograms show the background estimated from "mixed events".

The shape of the background under the proton, deuteron and triton signals in the M^2 spectra is estimated using the "mixed event" method. For that, tracks reconstructed in the central tracker are matched to hits in the ToF detectors taken from different events containing a similar number of tracks. The "mixed event" background is normalized to the integral of the signal histogram outside the M^2 windows of protons, deuterons and tritons. It is found that the background level differs for light and heavy targets and for different intervals of rapidity and transverse momentum.

(a) (b)

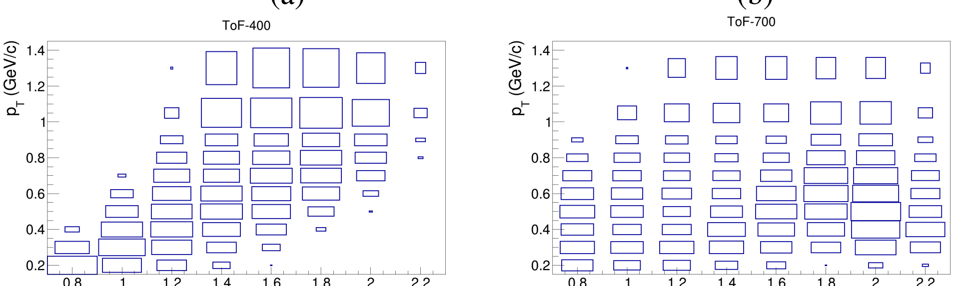

Figure 3. Distribution of the deuteron signals measured in ToF-400 (a) and ToF-700 (b) in the rapidity vs. transverse momentum plane in Ar+Sn interactions.

The ToF-400 and ToF-700 detectors cover different ranges of rapidity and transverse momentum of detected particles. Figure 3 shows the deuteron signals

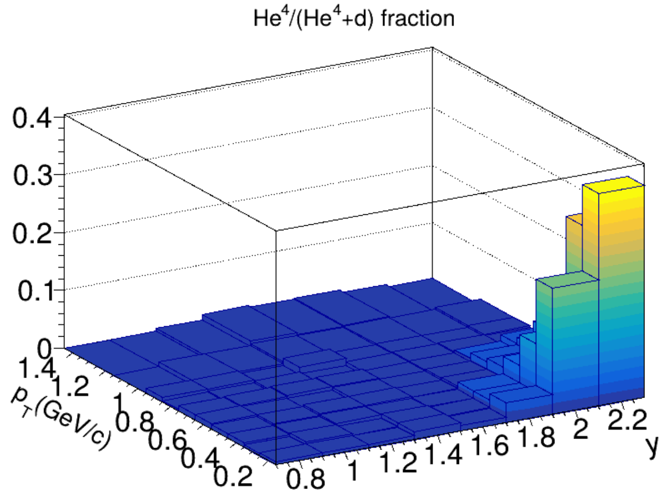

Figure 4. Fraction of He^4 in the $He^4 + d$ sample measured in the rapidity vs. transverse momentum plane in Ar+A interacions.

measured in ToF-400 and ToF-700 in the rapidity vs transverse momentum plane in Ar+Sn interactions before making efficiency corrections.

The dE/dx information from the GEM detectors is used to separate the deuteron signals from the overlapping TOF He^4 signals. The fraction of He^4 in the total $He^4 + d$ sample is determined in rapidity and transverse momentum bins and subtracted from the deuteron TOF signals. The He^4 fraction combined for all the targets is presented in figure 4. In most of the $y - p_T$ bins, the He^4 fraction does not exceed 3%. However, in a few bins at large y and low p_T, it reaches 20–35%.

4 Reconstruction efficiency and trigger performance

To evaluate the proton, deuteron and triton reconstruction efficiency, Monte Carlo data samples of argon-nucleus collisions were produced with the DCM-SMM event generator. The propagation of particles through the entire detector volume and responses of the detectors were simulated using the GEANT3 program [33] integrated into the BmnRoot software framework [34].

The Monte Carlo events passed through the same chain of reconstruction and identification as the experimental ones. The efficiencies of the silicon, GEM, CSC, DCH and ToF detectors were adjusted in the simulation in accordance with the measured detector efficiencies [35]. More details of the simulation are given in ref. [8].

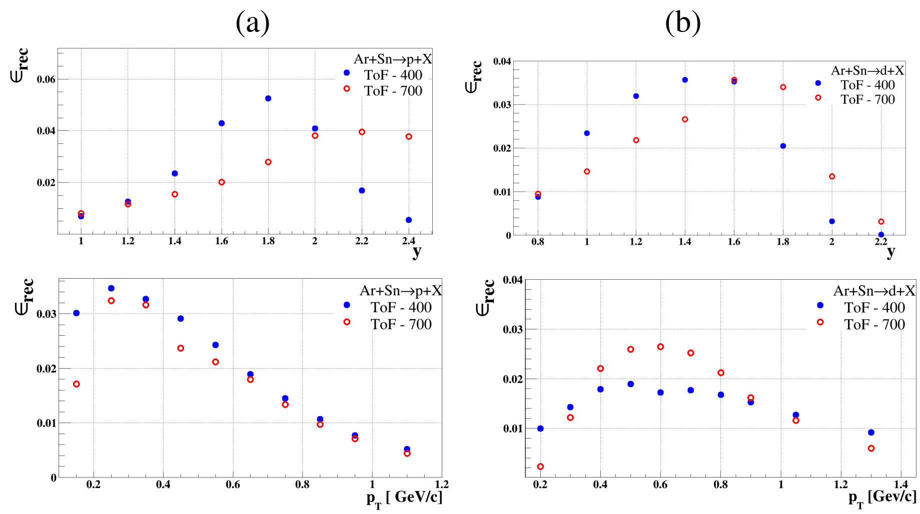

Figure 5. Reconstruction efficiency of protons (a) and deuterons (b) produced in Ar+Sn collisions, detected in ToF-400 (full blue circles) and ToF-700 (open red circles) as functions of rapidity y and p_T. The efficiency includes both acceptance and reconstruction.

The proton, deuteron and triton reconstruction efficiencies are calculated in intervals of rapidity y and transverse momentum p_T. The reconstruction efficiency includes geometrical acceptance, detector efficiency, kinematic and spatial cuts, and the loss of protons, deuterons and tritons due to in-flight interactions. Figure 5 shows the reconstruction efficiencies of protons (left panels) and deuterons (right panels) in ToF-400 and ToF-700 as functions of y (upper panels) and p_T (lower panels) for Ar+Sn interactions.

The trigger efficiency ϵ_{trig} depends on the number of fired channels in the BD (SiMD) detectors. It was calculated for events with reconstructed protons, deuterons and tritons using event samples recorded with an independent trigger based on the SiMD (BD) detectors. The BD and SiMD detectors cover different and non-overlapping regions of the BM@N acceptance, that is, they detect different collision products.

The efficiency of the combined BD and SiMD triggers was calculated as the product of the efficiencies of the BD and SiMD triggers. The trigger efficiency decreases with a decrease in the mass of the target and an increase in the centrality of the collision. More details of the trigger efficiencies evaluation are given in ref. [8]. In particular, the trigger system accepts events in the whole centrality range, as illustrated in figure 10 of [8].

5 Centrality classes

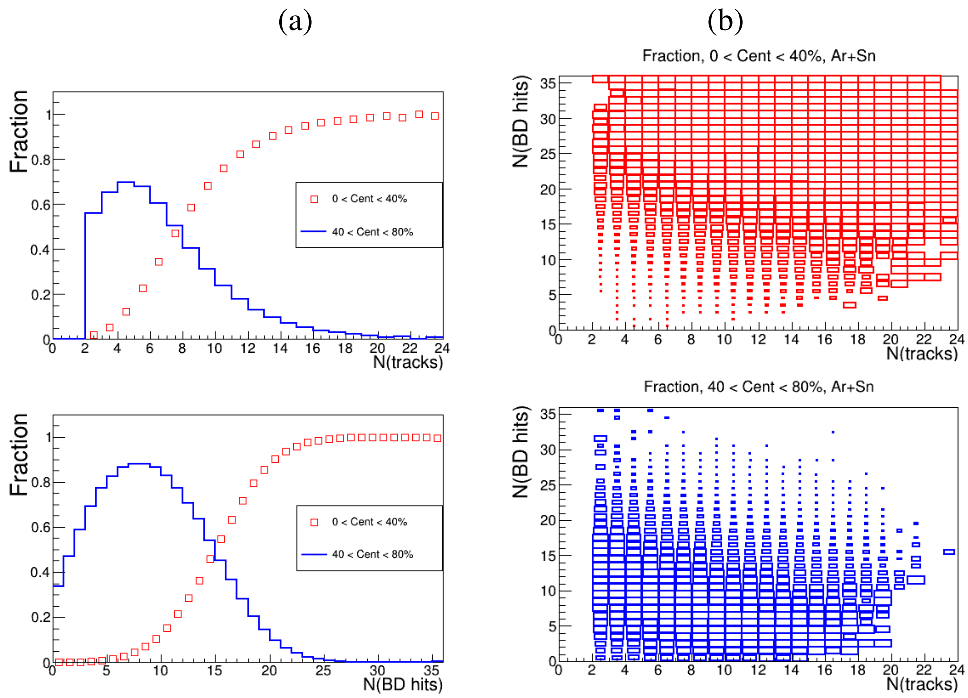

Figure 6. (a) Probability distribution of the number of tracks N(tracks) in the primary vertex (upper panel) and the number of hits N(BD) in the BD detector (lower panel) for events with centrality 0–40% (red open symbols) and 40–80% (blue histogram); (b) Two-dimensional plot of the probability distribution of N(tracks) (horizontal axis) vs. N(BD) (vertical axis) in events with centrality 0–40% (upper panel) and 40–80% (lower panel).

The event centrality is determined as the fraction of the interaction cross section in the impact parameter interval $[0, \mathrm{b}]$ of the nucleus-nucleus collision to the total inelastic interaction cross section. Two classes of centrality: 1) 0–40% of the cross section (more central collisions) and 2) 40–80% of the cross section (more peripheral collisions) are defined from the impact parameter distributions of Ar+A inelastic interactions simulated by the DCM-SMM model. The boundary impact parameters b_{40} and b_{80} for the definition of the two classes for interactions of Ar with various targets are given in table 1. It was found that the number of tracks originating from the primary event vertex N(tracks) and the number of hits in the Barrel Detector N(BD) are anti-correlated with the impact parameter b. Using results of the DCM-SMM Monte Carlo simulation, the fractions of reconstructed events, which belong to the centrality classes 0–40% and 40–80%, are calculated. Fractions of events with centrality 0–40% and 40–80% are presented in figure 6 as functions of N(tracks), N(BD) and as a two-dimensional distribution N(tracks) / N(BD).

Table 1. The boundary impact parameters b_{40} and b_{80} for the definition of the two centrality classes 0–40% and 40–80% and the inclusive inelastic cross section σ_{inel} for Ar+A interactions.

	Ar+C	Ar+Al	Ar+Cu	Ar+Sn	Ar+Pb
b_{40}, fm	4.23	4.86	5.66	6.32	7.10
b_{80}, fm	6.2	7.0	8.0	9.0	10.0
σ_{inel}, mb [36]	1470 ± 50	1860 ± 50	2480 ± 50	3140 ± 50	3940 ± 50

Fractions (probabilities) of events with centrality 0–40% and 40–80%, taken from the two-dimensional N(tracks)/N(BD) distributions, are used as event weights to define the weighted number of reconstructed protons, deuterons and tritons in the y and p_T bins in data and simulation. The systematic uncertainty of the event centrality is estimated from the remaining difference in the shape of the N(tracks) and N(BD) distributions in y and p_T bins in the simulation relative to the data.

6 Cross sections, multiplicities and systematic uncertainties

The protons, deuterons and tritons in Ar+C, Al, Cu, Sn and Pb interactions are measured in the following kinematic ranges: transverse momentum $0.1 < p_T < 1.2$ GeV/c (protons), $0.15 < p_T < 1.45$ GeV/c (deuterons), $0.2 < p_T < 1.6$ GeV/c (tritons) and rapidity in the laboratory frame $0.9 < y < 2.5$ (protons), $0.7 < y < 2.3$ (deuterons), $0.7 < y < 2.1$ (tritons). The differential cross sections $d^2\sigma_{p,d,t}(y, p_T)/dydp_T$ and multiplicities $d^2N_{p,d,t}(y, p_T)/dydp_T$ of protons, deuterons and tritons produced in Ar+C, Al, Cu, Sn and Pb interactions are calculated using the relations:

$$d^2\sigma_{p,d,t}(y,p_T)/dydp_T = \Sigma[d^2n_{p,d,t}(y,p_T,N_{tr})/(\epsilon_{trig}(N_{tr})dydp_T)] \times 1/(L\epsilon^{rec}_{p,d,t}(y,p_T))$$

$$d^2N_{p,d,t}(y,p_T)/dydp_T = d^2\sigma_{p,d,t}(y,p_T)/(\sigma_{inel}dydp_T), \tag{1}$$

where the sum is performed over bins of the number of tracks in the primary vertex; N_{tr}, $n_{p,d,t}(y,p_T,N_{tr})$ is the number of reconstructed protons, deuterons and tritons in the intervals dy and dp_T; $\epsilon_{trig}(N_{tr})$ is the track-dependent trigger efficiency; $\epsilon^{rec}_{p,d,t}(y,p_T)$ is the reconstruction efficiency of protons, deuterons and tritons; L is the luminosity; and σ_{inel} is the inelastic cross section for argon-nucleus interactions. The cross sections and multiplicities are evaluated for the two centrality classes: 0–40% and 40–80%.

Table 2. Mean systematic uncertainties averaged over the y, p_T ranges of protons, deuterons and tritons measured in argon-nucleus interactions.

	Ar+C %	Ar+Al %	Ar+Cu %	Ar+Sn %	Ar+Pb %
ϵ_{trig} p,d,t	9	7	7	7	7
protons					
n_p/ϵ_{rec}	15	6	8	14	11
Total	18	9	11	16	13
deuterons					
n_d/ϵ_{rec}	32	22	20	19	22
Total	33	23	21	20	23
tritons					
n_t/ϵ_{rec}	43	22	20	20	22
Total	44	23	21	21	23

Several sources are considered for evaluating the systematic uncertainty of the proton, deuteron and triton yield $n_{p,d,t}$ and the reconstruction efficiency ϵ_{rec}. Some of them affect both the yield $n_{p,d,t}$ and the reconstruction efficiency, ϵ_{rec}. For these cases, the correlated effect is taken into account by considering the variations on the $n_{p,d,t}/\epsilon_{rec}$ ratio. A detailed discussion of the systematic uncertainties associated with track reconstruction as well as trigger efficiency is given in ref. [8]. Additional sources specific to this analysis are listed below:

- Systematic uncertainty of the background subtraction in the mass-squared M^2 spectra of identified particles: it is estimated as the difference between the background integral under the p, d, t mass-squared windows taken from "mixed events" (as described in section 3) and from the fitting of the M^2 spectra by a linear function. The latter is done in the M^2 range, excluding the proton, deuteron and triton signal windows.

- Systematic uncertainty calculated as half of the difference between the p/d/t yield measured in the ToF-400 and ToF-700 detectors in bins of rapidity y.
- Systematic uncertainty of the event centrality weights estimated 1) from the remaining difference in the shape of the N(track) and N(BD) distributions in y and p_T bins in the data and the simulation; 2) from the difference in the event centrality weights taken from the two-dimensional N(track) / N(BD) distribution relative to the one-dimensional N(BD) distribution.

Table 2 summarizes the mean values (averaged over p_T, y and N_{tr}) of the systematic uncertainties of the various factors of eq. 1, $n_{p,d,t}$, ϵ_{rec}, and ϵ_{trig}. The total systematic uncertainty from these sources, calculated as the square sum of their uncertainties from different sources, is listed in table 2 for each target.

The luminosity is calculated from the beam flux Φ as given by the beam trigger (see section 2) and the target thickness l using the relation $L = \Phi\rho l$, where ρ is the target density expressed in atoms/cm^3. The systematic uncertainty of the luminosity is estimated from the fraction of the beam that can miss the target, determined from the vertex positions, and found to be within 2%. The inelastic cross sections of Ar+C, Al, Cu, Sn and Pb interactions are taken from the predictions of the DCM-SMM model. The σ_{inel} uncertainties for Ar+C, Al, Cu, Sn and Pb interactions given in table 1 are estimated from the empirical formulas taken from ref. [36, 37].

7 Rapidity and transverse mass spectra

At a kinetic energy of 3.2 A GeV, the rapidity of the nucleon-nucleon center-of-mass (CM) system is $y_{CM} = 1.08$. The rapidity intervals covered in the present measurements, $0.9 < y < 2.5$, $0.7 < y < 2.3$ and $0.7 < y < 2.1$ for protons, deuterons and tritons, respectively, correspond therefore to the forward and central rapidity regions in the nucleon-nucleon CM system. The measured yields of protons, deuterons and tritons in m_T and y bins in the two centrality intervals in Ar+C, Al, Cu, Sn and Pb interactions can be found in ref. [38].

As an example, figure 7 shows the invariant transverse mass $m_T = \sqrt{m^2 + p_T^2}$ spectra of protons, deuterons and tritons ($m = m_{p,d,t}$) produced in various targets

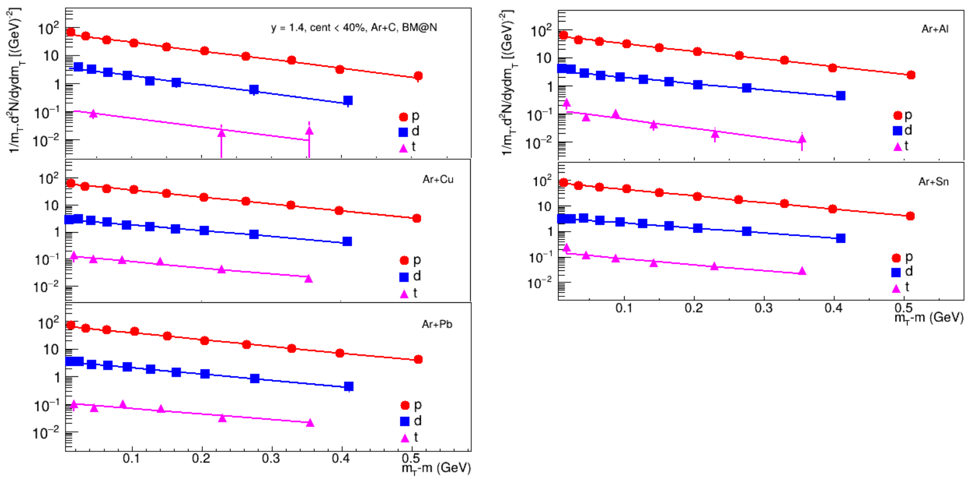

Figure 7. Invariant transverse mass spectra of protons, deuterons and tritons produced at rapidity $y = 1.4$ in Ar+C, Al, Cu, Sn and Pb interactions with centrality 0–40%. The vertical bars and boxes represent the statistical and systematic uncertainties, respectively. The lines show the results of the fit by an exponential function.

at $y = 1.4$ in the 0–40% centrality class. The spectra are parameterized by an exponential function as:

$$\frac{1}{m_T} d^2N/dydm_T = \frac{dN/dy}{T_0(T_0+m)} \exp(-(m_T - m)/T_0), \tag{2}$$

where the fitting parameters are the integral of the m_T spectrum, dN/dy, and the inverse slope, T_0. The dN/dy and T_0 values extracted from the fit can be found in ref. [38]. The dN/dy distributions of protons, deuterons and tritons produced in collisions with centrality 0–40% in the various targets are shown in figures 8(a), 9(a) and 10(a), respectively. The figures also show the comparison of the results with predictions of the DCM-SMM and PHQMD models. The boundary impact parameters b_{40} and b_{80} from table 1 are used for the definition of the centrality classes in the models.

It is seen that the shapes of the particle rapidity density vary strongly with the target mass. For protons, the models have quite similar predictions, which are in reasonable agreement with the experimental results in the forward rapidity range except for Ar+C interactions, where the models underestimate the absolute yields of data.

Deuterons and tritons are predominantly produced in the beam fragmenta-

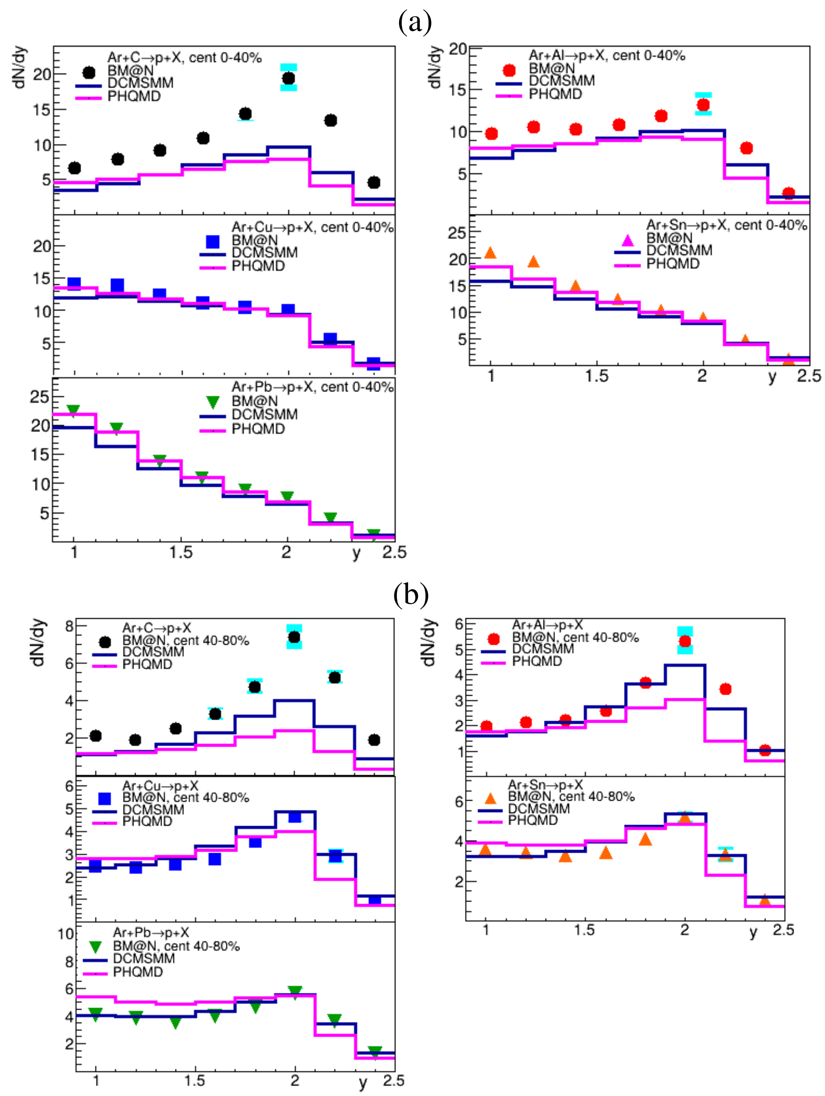

Figure 8. Rapidity distributions dN/dy of protons produced in Ar+C, Al, Cu, Sn and Pb interactions at 3.2 A GeV with centrality 0–40% (a) and 40–80% (b). The results are integrated over p_T. The vertical bars and boxes represent the statistical and systematic uncertainties, respectively. The predictions of the DCM-SMM and PHQMD models are shown as blue and magenta lines.

(a)

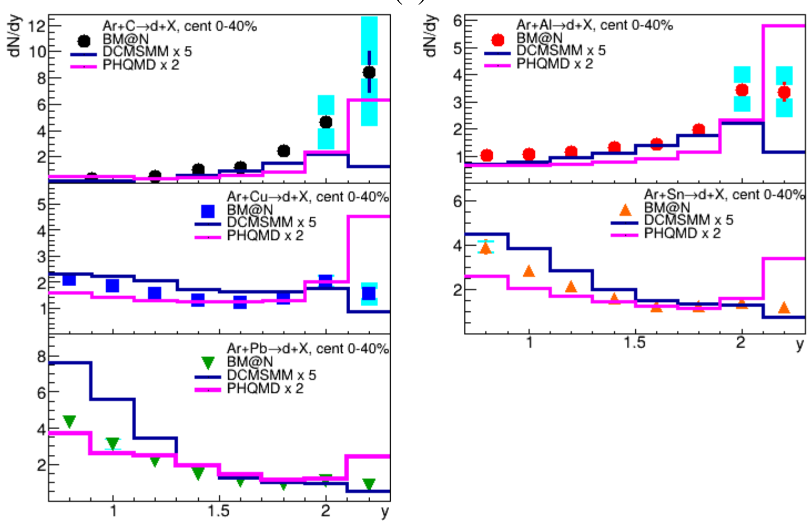

(b)

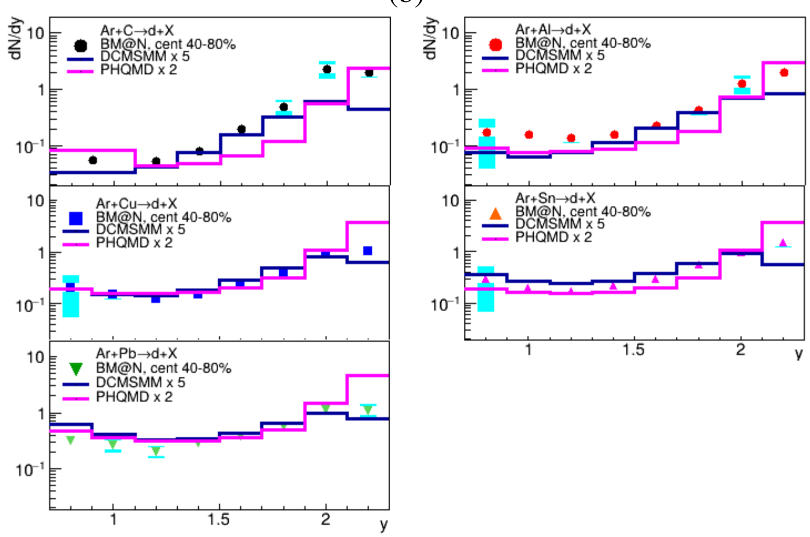

Figure 9. Rapidity distributions dN/dy of deuterons produced in Ar+C, Al, Cu, Sn and Pb interactions with centrality 0–40% (a) and 40–80% (b). The results are integrated over p_T. The vertical bars and boxes represent the statistical and systematic uncertainties, respectively. The predictions of the DCM-SMM and PHQMD models, multiplied by factors of 5 and 2, respectively, are shown as blue and magenta lines.

(a)

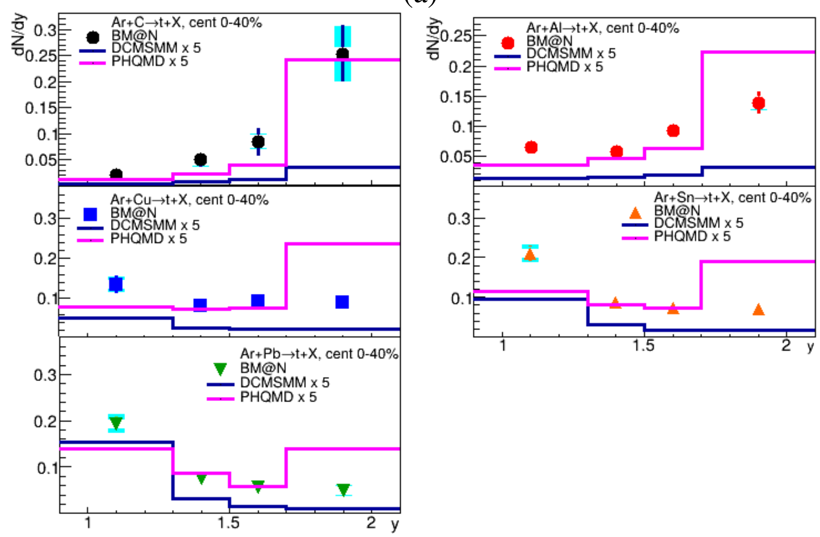

(b)

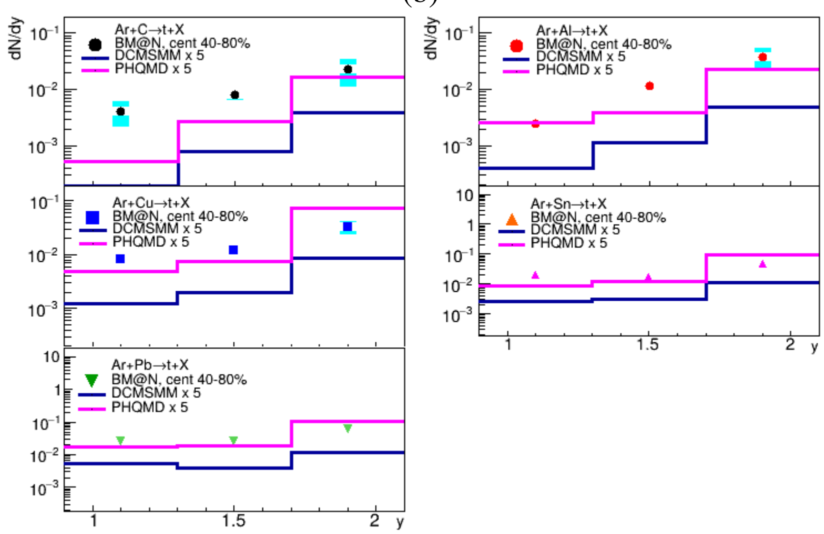

Figure 10. Rapidity distributions dN/dy of tritons produced in Ar+C, Al, Cu, Sn and Pb interactions with centrality 0–40% (a) and 40–80% (b). The results are integrated over p_T. The vertical bars and boxes represent the statistical and systematic uncertainties, respectively. The predictions of the DCM-SMM and PQHMD models, multiplied by a factor of 5, are shown as blue and magenta lines.

tion region for Ar+C and Ar+Al interactions, whereas for heavier targets they are mostly produced at mid-rapidity. For deuterons, the DCM-SMM and PHQMD models reasonably describe the shape of the experimental spectra but under-predict the absolute yields by factors of about 5 and 2, respectively. The triton yields predicted by the models are below the experimental data by a factor of about 5.

The dN/dy distributions vs y of protons, deuterons and tritons produced in collisions with centrality 40–80% on the various targets are shown in figures 8(b), 9(b) and 10(b), respectively. The largest contribution is observed in the beam fragmentation region for all the targets. This tendency is reproduced by the DCM-SMM and PHQMD models. Again, the models underestimate the absolute yields for deuterons by factors of 5 and 2, respectively. The triton yields predicted by the models are below the experimental data by a factor of about 5. A significant deficit of deuterons and tritons in the PHQMD model relative to the experimental data has also been observed in central (0–10%) collisions of Au+Au at $\sqrt{s_{NN}}$ of 3 GeV by the STAR experiment [39].

The observed discrepancy between the data and the DCM-SMM and PHQMD models could be partially explained by feed-down from excited nuclear states, which are not taken into account in the models. At BM@N collision energies, the reaction zone consists of a hadronic gas dominated by nucleons and stable nuclei (d, t, He^3, He^4). However, in addition to these, there are many excited nuclear states with mass number $A \geqq 4$. The role of the feed-down from these states for the description of light nuclei production in a broad energy range was discussed in ref. [40]. As reported in [40], feeding gives a significant contribution to the yields of d, t at NICA/BM@N energies: as much as 60% of all final tritons and 20% of deuterons may come from the decays of excited nuclear states.

The mean transverse kinetic energy, defined as $\langle E_T \rangle = \langle m_T \rangle - m$, is related to the T_0 value extracted from the fit of the m_T spectrum by the following equation:

$$\langle E_T \rangle = \langle m_T \rangle - m = T_0 + T_0^2/(T_0 + m). \tag{3}$$

The $\langle E_T \rangle$ values of protons in the 0–40% centrality class are shown in figure 11(a) as a function of rapidity. The maximal values of $\langle E_T \rangle$ are measured at rapidity $1.0 < y < 1.3$, i.e., at mid-rapidity in the CM system. In general, the y dependence of $\langle E_T \rangle$ for protons is consistent with predictions of the DCM-SMM and PHQMD models.

The $\langle E_T \rangle$ values for deuterons and tritons in the 0–40% centrality class are shown as functions of rapidity in figures 11(b) and 11(c), respectively. PHQMD reproduces the rise of the data at mid-rapidity in CM for deuterons and tritons

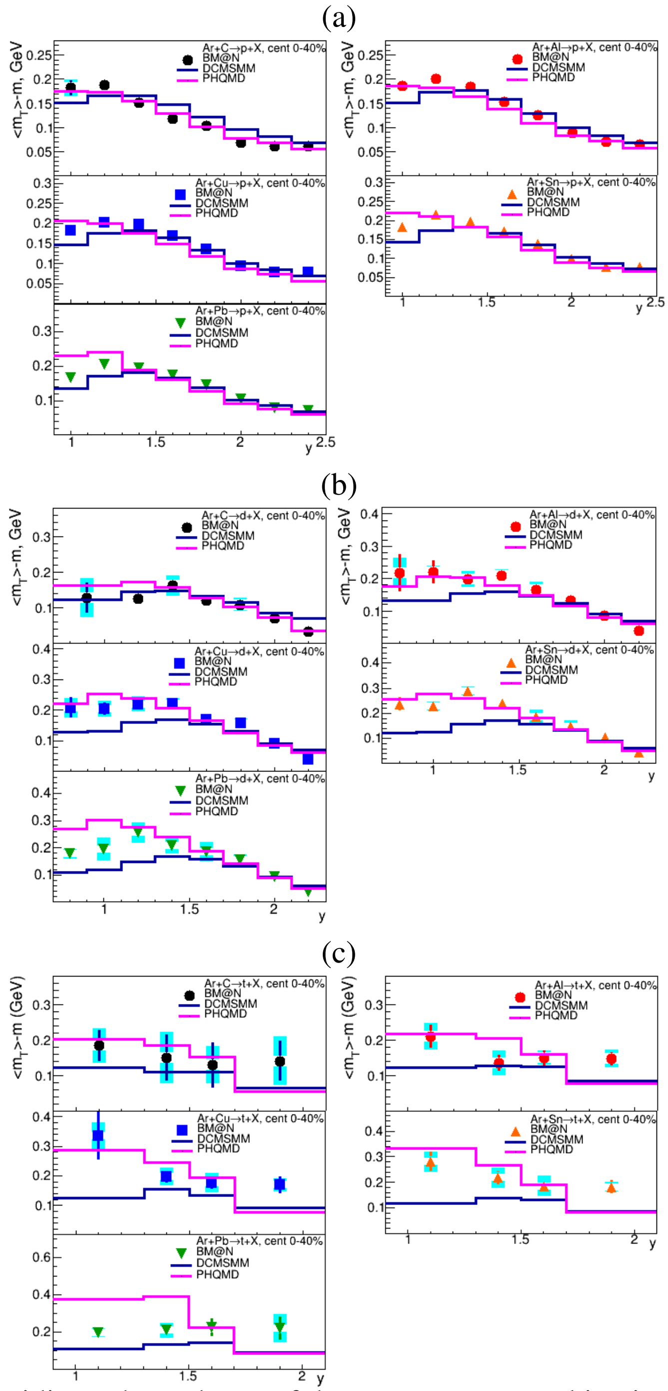

Figure 11. Rapidity y dependence of the mean transverse kinetic energy $\langle E_T \rangle = \langle m_T \rangle - m$ of protons (a), deuterons (b) and tritons (c) in Ar+C, Al, Cu, Sn and Pb interactions with centrality 0–40%. The vertical bars and boxes represent the statistical and systematic uncertainties, respectively. The predictions of the DCM-SMM and PHQMD models are shown as blue and magenta lines.

relative to protons, whereas the DCM-SMM model predicts similar $\langle E_T \rangle$ values for protons, deuterons and tritons contrary to the experimental results.

A Blast-Wave model [48] was used to fit the invariant transverse mass spectra of protons, deuterons and tritons according to a formula valid on the assumption of a box-like density profile with a uniform density inside the fireball (thermal source) region of transverse radius $r \leq R$:

$$\frac{d^2N}{m_T dm_T dy} = Norm(y) \int_0^R m_T K_1 \Big(\frac{m_T \cosh \rho(r)}{T} \Big) I_0 \Big(\frac{p_T \sinh \rho(r)}{T} \Big) r dr, \quad (4)$$

where $Norm(y)$ is the normalization factor, I_0 and K_1 are the modified Bessel functions, T is the kinetic freeze-out temperature and $\rho(r) = \tanh^{-1} \beta(r)$ is the transverse radial flow rapidity profile. The transverse radial flow velocity $\beta(r)$ inside the fireball region is usually parametrized as $\beta = \beta_s (r/R)^n$, where β_s is the fireball-surface velocity. Assuming a linear velocity profile (exponent $n = 1$), one gets an average transverse radial flow velocity $\langle \beta \rangle = (2/3)\beta_s$. Figure 12 shows the invariant m_T-spectra of p, d, t produced at rapidity $y = 1.4$ in Ar+C, Al, Cu, Sn and Pb interactions with centrality 0–40%. The BM@N data are shown by symbols, the Blast-Wave model motivated fits are drawn by lines. The average radial flow velocity $\langle \beta \rangle$ and source temperature T at the kinetic freeze-out extracted from the Blast-Wave model fits to the transverse mass spectra of protons, deuterons and tritons measured in the range $0.9 < y < 1.5$ ($-0.18 < y^* < 0.42$ in the center-of-mass system) are given in table 3. The quadratic sum of the statistical and systematical uncertainties of data points are used to evaluate the errors of the fit parameters. The parameters of the fit were assumed to be constant in the rapidity range of the fit. If a functional form of the Boltzmann approximation $T(0)/\cosh y^*$ with the midrapidity temperature $T(0)$ is used instead, the difference in the fit result is within 5%.

One may also obtain the temperature T and mean transverse radial flow velocity $\langle \beta \rangle = 2/(n+2)\beta_s$ from common fits of transverse kinetic energies $\langle E_T \rangle$ of protons, deuterons and tritons using the formula following from eq. 4 in the limit of small $1/z = T/m$ and β_s^2:

$$\begin{aligned}\langle E_T \rangle = T\Big(&[1 + 3/(2z) - 9/(8z^2)] + \beta_s^2 z[(1+1/z)(1+3/z) - 9/(2z^3)]/[2(n+1)] + \\ &+ \beta_s^4 z[(3 + n(6+5n)) + (9 + n(18+17n))/z + 3(3 + n(6+7n))/(8z^2) - \\ &- 9(1 + n(2+9n))/(8z^3)]/[8(1+n)^2(1+2n)]\Big), \quad (5)\end{aligned}$$

valid up to terms $O(1/z^3)$ and $O(\beta_s^6)$. Note that at temperatures T of a hundred MeV, the β_s^2-term in eq. 5 is nearly linear in the cluster mass m down to proton mass. The fitted parameters agree with those in table 3, except for approximately 50% higher errors due to the integration over $\langle E_T \rangle$ of part of the information contained in the m_T spectra.

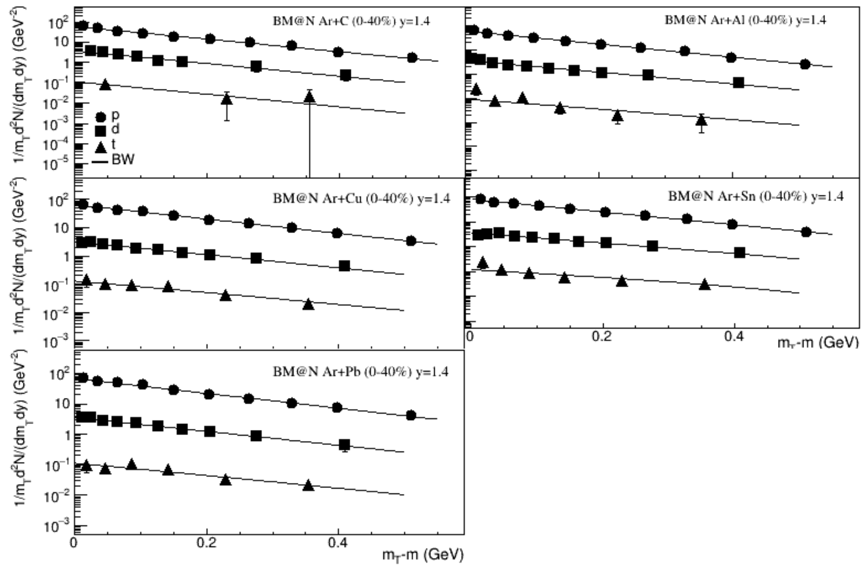

Figure 12. Invariant m_T-spectra of p, d, t produced at rapidity $y = 1.4$ in 0–40% central Ar+A interactions. The BM@N data are shown by symbols, the Blast-Wave model motivated fits are drawn by lines.

One finds a flow velocity consistent with zero in central Ar+C collisions. Nuclear collisions of such small systems can be considered as a superposition of independent nucleon-nucleon interactions; therefore, the density of participants reached in these reactions is probably not high enough to create a fireball with strong collective behavior. In contrast, for larger colliding systems (Ar+Al, Cu, Sn and Pb), the particle density and re-scattering rate inside the reaction zone are higher, giving rise to a collective flow velocity. It appears that the observed target mass dependence for T and $\langle \beta \rangle$ is weak at BM@N energies: fitted temperature and mean flow velocity are practically the same within the errors for studied colliding systems. This might be an indication that the increase of the reaction volume and the number of collisions with the target mass is not accompanied by a significant compression of the nuclear matter.

The BM@N results for kinetic freeze-out parameters (T_{kin} and $\langle \beta \rangle$) could be compared with measurements at lower and higher energies. Figure 13 presents results for centrality-selected nucleus-nucleus collisions from the BM@N experiment (this study, 0–40% central Ar+A at $\sqrt{s_{NN}} = 3.1$ GeV), the EOS experi-

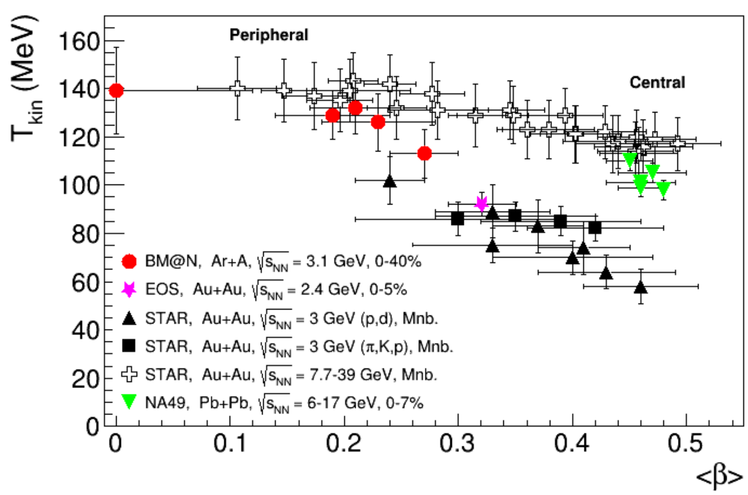

Figure 13. Kinetic freeze-out parameters (T_{kin} and $\langle\beta\rangle$) in centrality selected nucleus-nucleus collisions: Ar+A (this study); Au+Au from EOS [44] and STAR [45–47]; Pb+Pb from NA49 [42]. For the STAR results, “Mnb.” stands for minimum bias, the label “Peripheral” and “Central” indicates the most peripheral (70–80% central) and the most central (0–5% central) bins of Au+Au collisions, respectively.

ment [44] (0–5% central Au+Au at $\sqrt{s_{NN}} = 2.4$ GeV), the STAR experiment [45, 46] (0–5%, 5–10%, 10–20%,...,70–80% central Au+Au at $\sqrt{s_{NN}} = 7.7$–39 GeV), and the NA49 experiment [42] (0–7% central Pb+Pb at $\sqrt{s_{NN}} = 6.2$–17.3 GeV). Preliminary STAR results from a Blast-Wave analysis of hadron and light nuclei spectra in centrality-selected Au+Au collisions at $\sqrt{s_{NN}}$ = 3 GeV [47] are also presented. These results are shown for different combinations of particle species used in the Blast-Wave fits: light hadrons (π, K, p) or protons and deuterons (p, d). Thought the quoted uncertainties in a BW-motivated analysis are big, there is an indication that the system size trend for kinetic freeze-out parameters is different in low ($\sqrt{s_{NN}} < 6$ GeV) and high-energy collisions.

Table 3. T and $\langle\beta\rangle$ values evaluated from the Blast-Wave fit of the transverse mass spectra of protons, deuterons and tritons produced in the rapidity range $-0.18 < y^* < 0.42$ in Ar+A interactions with centrality 0–40%. The errors represent the uncertainties of the fit to the data points with the quadratic sum of the statistical and systematical uncertainties.

	Ar+C	Ar+Al	Ar+Cu	Ar+Sn	Ar+Pb
T , MeV	140 ± 18	129 ± 10	132 ± 11	113 ± 10	126 ± 12
$\langle\beta\rangle$	$0.0\pm^{0.12}_{0.0}$	0.19 ± 0.05	0.21 ± 0.04	0.27 ± 0.03	0.23 ± 0.05
χ^2/ndf	44/49	127/55	113/55	86/55	172/55

8 Coalescence factors

Within a coalescence model [18, 19, 21], nuclear fragment formation is characterized by a coalescence factor B_A, defined through the invariant momentum spectra by the equation:

$$E_A d^3N_A/d^3p_A = B_A(E_p d^3N_p/d^3p)^Z (E_n d^3N_n/d^3p)^{A-Z}_{|p=p_A/A} \,,$$

where p_A and $p = p_A/A$ are momenta of the nuclear fragment A and the nucleon, respectively. It relates the yield N_A of nuclear fragments with charge Z and atomic mass number A to the yields of the coalescing nucleons N_p and N_n at the same velocity. Assuming that neutron momentum density is equal to the proton momentum density at freeze-out, the B_A value can be calculated as:

$$B_A = d^2N_A/2\pi p_{T,A}dp_{T,A}dy/(d^2N_p/2\pi p_T dp_T dy)^A/(n/p)^{A-Z}, \quad (6)$$

where n/p is the ratio of the numbers of produced neutrons to protons. The coalescence factor is inversely related to the effective emission volume of the nucleons with nearby 3-momenta [21]: $B_A \sim V_{eff}^{1-A}$. The strong position-momentum correlations present in the expanding source lead to a higher coalescence probability at larger p_T values. Assuming a box-like transverse density profile of the source, the model predicts at small or moderate p_T [22]:

$$B_A \simeq g_s \Lambda_A A^{-1/2} C_A[(2\pi)^{3/2}/(m_T R_{\|}(m_T) R_{\perp}^2(m_T))]^{A-1} \exp[m_T(1/T_p - 1/T_A)], \quad (7)$$

where $g_S = (2S+1)/2^A$ is the spin factor of the nuclear fragment A, Λ_A is a suppression factor of correlated nucleons, e.g., due to a feed-down fraction of uncorrelated nucleons produced in hyperon decays, C_A is a quantum correction factor related to the finite fragment size [21, 22], $R_{\perp}$ and $R_{\|}$ are the femtoscopic radii of the source in the longitudinally co-moving system (LCMS) [22], T_p and T_A are the inverse transverse momentum slopes for proton and fragment A, respectively. The Λ_A factor is close to 1 in the BM@N energy range, as the fraction of nucleons originated from hyperon decays is around 2% according to predictions of the UrQMD model [61]. The UrQMD and PHQMD models predict the n/p ratio to be between 1.09 and 1.18 in the BM@N rapidity range for Ar+C and Ar+Pb interactions, respectively (see also section 9).

Figures 14(a) and 14(b) show the B_2 and B_3 values as functions of the transverse momentum measured in argon-nucleus interactions with centrality 0–40%. The transverse momentum is scaled to the atomic number of the nuclear fragment (deuteron, triton), p_T/A. The yields of protons (N_p), deuterons (N_d) and tritons (N_t) are measured in the same rapidity range, namely $0.9 < y < 1.7(-0.18 < y^* < 0.62)$. The statistics of tritons is not sufficient to present B_3 for Ar+C interactions. It is found that B_2 and B_3 rise with p_T at low p_T and saturate at higher p_T for all the measured targets. The B_2 and B_3 values at low p_T are smaller for heavier targets compared to lighter targets.

In order to compare the present measurements of B_2 and B_3 with previously obtained results, the $B_2(p_T)$ and $B_3(p_T)$ values given in figures 14(a) and 14(b) are extrapolated down to $p_T = 0$ using exponential fits of the form $b\exp[a(m_T - m_A)]$ as predicted by the coalescence model with a box-like density profile [22] (see eq. 7). The fits are performed for the first four data points in the range $p_T/A < 0.32$. is scaled up by a factor $\sqrt{\chi^2/ndf}$ following recommendation in ref. [51]. The results of the extrapolation are given in table 4.

(a)

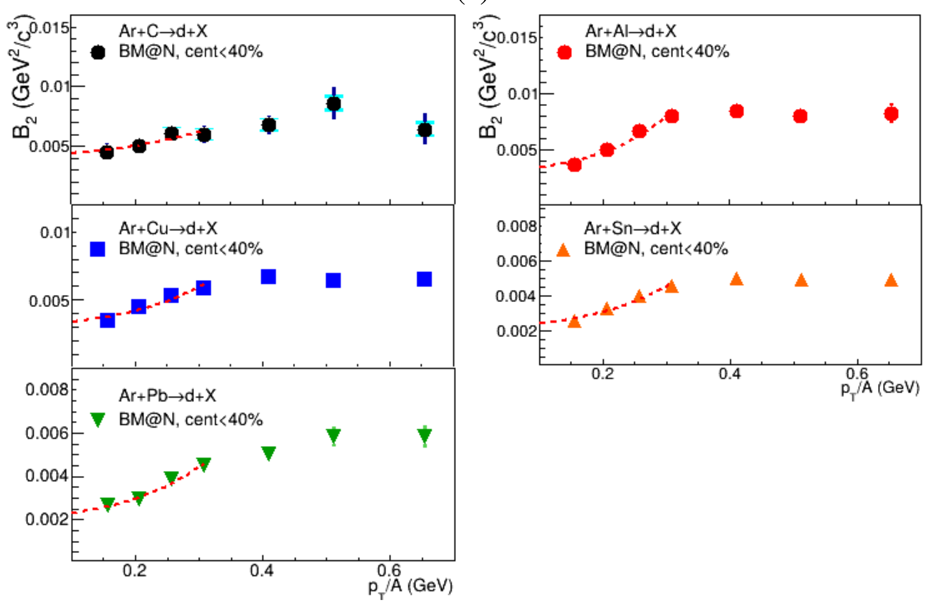

(b)

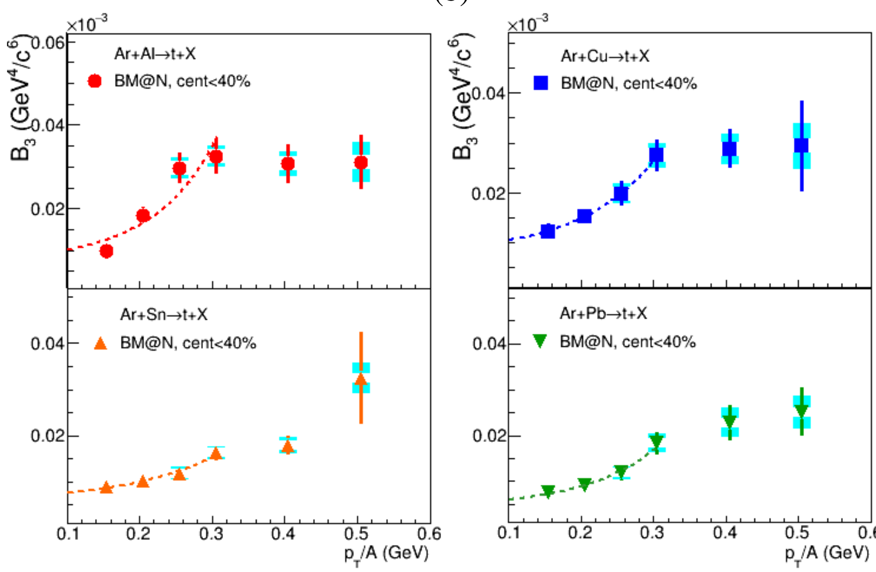

Figure 14. Coalescence parameter B_2 for deuterons (a) and B_3 for tritons (b) measured as a function of p_T/A in the rapidity range $-0.18 < y^* < 0.62$ in Ar+A collisions with centrality 0–40%. Dash lines show results of the fits in the range $p_T/A < 0.32$ described in the text.

Table 4. Coalescence parameters $B_2(p_T = 0)$ and $B_3(p_T = 0)$ extrapolated to $p_T = 0$ using an exponential fit to $B_2(p_T)$ and $B_3(p_T)$; coalescence radii $R^d_{coal}(p_T = 0)$ and $R^t_{coal}(p_T = 0)$ evaluated from the $B_2(p_T = 0)$ and $B_3(p_T = 0)$ values for deuterons and tritons produced in the rapidity ranges $-0.18 < y^* < 0.22$ and $0.22 < y^* < 0.62$ in Ar+A interactions with centrality 0–40%. The quoted errors are the quadratic sums of the statistical and systematic uncertainties.

	Ar+C	Ar+Al	Ar+Cu	Ar+Sn	Ar+Pb
$-0.18 < y^* < 0.22$					
$B_2(p_T = 0)/10^3$, GeV^2/c^3	2.8 ± 0.9	1.95 ± 0.7	2.6 ± 0.3	1.8 ± 0.2	1.35 ± 0.2
$B_3(p_T = 0)/10^6$, GeV^4/c^6		7.2 ± 2.2	5.8 ± 2.8	4.9 ± 0.6	2.6 ± 0.4
$R^d_{coal}(p_T = 0)$, fm	2.4 ± 0.3	2.7 ± 0.3	2.5 ± 0.2	2.8 ± 0.2	3.1 ± 0.2
$R^t_{coal}(p_T = 0)$, fm		2.4 ± 0.2	2.5 ± 0.2	2.5 ± 0.2	2.9 ± 0.2
$0.22 < y^* < 0.62$					
$B_2(p_T = 0)/10^3$, GeV^2/c^3	3.54 ± 0.9	3.56 ± 0.5	3.0 ± 0.8	2.06 ± 0.5	2.67 ± 0.4
$B_3(p_T = 0)/10^6$, GeV^4/c^6		9.6 ± 3.0	9.3 ± 2.9	7.3 ± 2.7	5.1 ± 2.3
$R^d_{coal}(p_T = 0)$, fm	2.2 ± 0.2	2.2 ± 0.2	2.4 ± 0.2	2.7 ± 0.2	2.5 ± 0.2
$R^t_{coal}(p_T = 0)$, fm		2.2 ± 0.2	2.3 ± 0.2	2.4 ± 0.2	2.5 ± 0.2

(a)

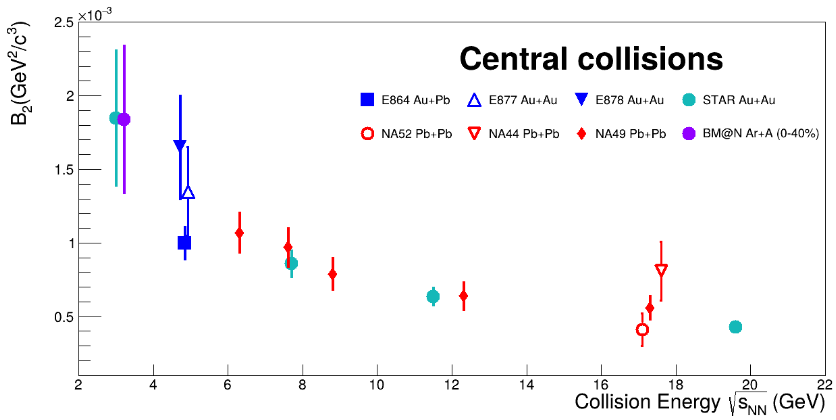

(b)

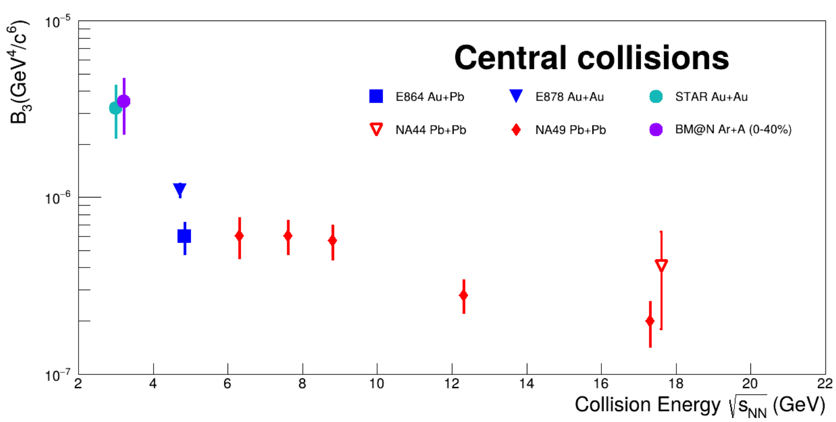

Figure 15. Coalescence parameters $B_2(p_T = 0)$ (a) and $B_3(p_T = 0)$ (b) for deuterons and tritons as a function of the nucleon-nucleon center-of-mass energy. The BM@N result is the weighted average value calculated in the rapidity range $-0.18 < y^* < 0.22$ for Ar+Al, Cu, Sn and Pb interactions with centrality 0–40%.

The BM@N values of $B_2 = 1.84 \pm 0.5$ GeV^2/c^3 and $B_3 = 3.5 \pm 1.2$ GeV^4/c^6 calculated as the weighed average values for Ar+Al, Cu, Sn and Pb interactions with centrality 0–40% are compared in figure 15 (a), (b) with the measurements of other experiments: STAR (0–10% central, $p_T/A = 0.65$ GeV/c) [39, 57, 58], NA44 (0–10% central) [52], NA52 [56], E864 [53], E877 [54], E878 [55] (0-10% cental), NA49 (0–7% central) [42]. The B_2 and B_3 results for Ar+A interactions with centrality 0–40% are consistent with the general trend of decreasing B_2 and B_3 values with rising collision energy of central interactions of heavy nuclei. The B_2 and B_3 values are inversely related to the coalescence radius R_{coal}, which is closely related to the LCMS femtoscopic radii of the source $R_{out}, R_{side}, R_{long} = R_{\|}$ with $R_{out}(p_T = 0) = R_{side}(p_T = 0) = R_{\perp}$ [22]. Based on eq. 7 at $p_T = 0$, one can define $R_{coal} = \sqrt[3]{R_{\|} R_{\perp}^2}$ and calculate it from the $B_2(p_T = 0)$ and $B_3(p_T = 0)$ values of deuterons and tritons. In the calculations, the C_d and C_t factors from [52] are scaled according to the mass of the colliding systems to account for the suppression related to the increased effective volume due to the finite deuteron and triton radii (see eq. 4.12) in [22]). The resulting values are in the range of 0.55–0.61 and 0.51–0.58 for C_d and C_t, respectively. The results for R_{coal} are given in table 4.

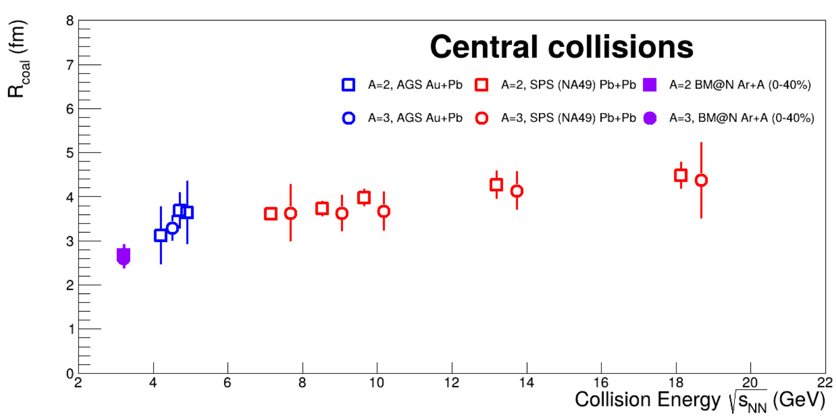

Figure 16. Coalescence radii R_{coal} for deuterons and tritons as a function of the nucleon-nucleon center-of-mass energy. The BM@N result is the weighted average value calculated in the rapidity range $-0.18 < y^* < 0.22$ for Ar+Al, Cu, Sn and Pb interactions with centrality 0–40%.

The coalescence source radii for deuterons and tritons produced in Ar+Al, Cu, Sn and Pb interactions with centrality 0–40% are consistent within the errors.

The BM@N values for the coalescence radii averaged for Ar+Al, Cu, Sn and Pb interactions are compared in figure 16 with results at higher energies and larger collision systems as compiled in [42]. Figure 15 exhibits a weak increase of the coalescence radii as a function of the center-of-mass energy in the nucleon-nucleon system. The BM@N results reported here are consistent with no or weak dependence of R_{coal} on target size within the experimental uncertainties.

9 Baryon rapidity distributions, stopping and rapidity loss in Ar+A

The total baryon number at a given rapidity in Ar+A collisions at NICA/BM@N energies is basically determined by the nucleons and the light nuclei ($d, t,$^{3}He). According to the results on the rapidity spectra of protons and light nuclei presented in section 7, the number of nucleons bound in clusters contributes to the total number of baryons up to about 15% and 25% in central Ar+C and Ar+Pb reactions, respectively. To obtain the baryon rapidity distribution, we add up the baryon number of the measured protons, deuterons and tritons in every rapidity bin. The obtained distribution is then corrected for unmeasured baryons: neutrons, hyperons and ^{3}He nuclei. Calculations with the PHQMD and UrQMD models indicate that for all collision systems, the n/p ratio is about 1.1 in the forward hemisphere, varying slowly with rapidity and then increasing abruptly to ≈1.22 (the n/p ratio in the projectile Ar nucleus) at the beam rapidity. We use these model predictions to estimate the yield of neutrons n; furthermore, we assume that the $t/^3$He ratio is equal to n/p. Hyperons contribute less than 2% to the total baryon number according to the PHQMD and UrQMD [61] models and are thus neglected. The total number of baryons B in a rapidity bin is then calculated as

$$B = p + n + 2.0 \cdot d + 5.7 \cdot t,$$

where the coefficient in front of t is 5.7 = 3.0 (for tritons) + 3.0/1.1 (for ^{3}He). The resulting baryon rapidity distributions for Ar+Cu collisions are shown in figure 17 as a function of the rapidity in the center-of-mass system y^*: the left panel shows the results for 0–40% central collisions, and the right one is for 40–80% central collisions. A large difference in the shapes of the dn/dy distributions is observed as more baryons are transported to midrapidity in the more central collisions. To describe those shapes, we fitted the measurements to a 3^{rd} order polynomial in

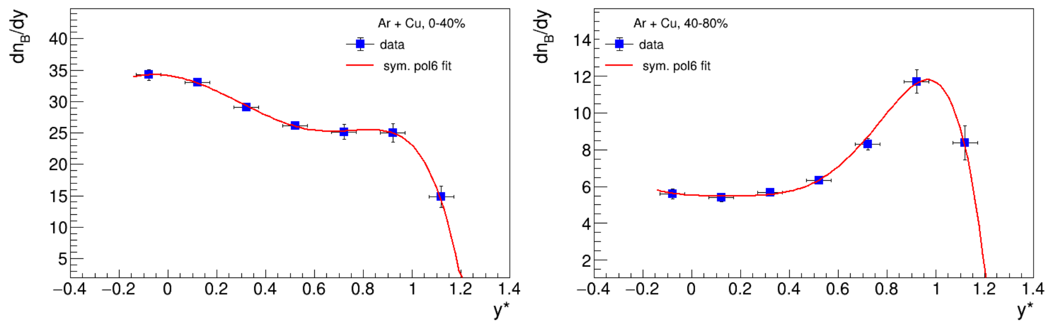

Figure 17. Left: Rapidity distribution of baryons in 0–40% central Ar+Cu collisions. The measurements are shown by solid dots, whereas the solid line represents the results of a fit to a 3^{rd} order polynomial in y^{*2}. Right: same for 40–80% central Ar+Cu collisions.

Table 5. The average rapidity loss $\langle \delta y \rangle$ in Ar+A reactions. The quoted uncertainties are statistical errors.

	Ar+C	Ar+Al	Ar+Cu	Ar+Sn	Ar+Pb
0-40%	0.42 ± 0.04	0.50 ± 0.03	0.58 ± 0.02	0.63 ± 0.02	0.65 ± 0.02
40-80%	0.38 ± 0.04	0.41 ± 0.04	0.45 ± 0.03	0.47 ± 0.03	0.48 ± 0.04

y^{*2} (as suggested in ref. [59]), and the fit results are shown in figure 17 by solid curves.

The average rapidity loss is calculated as (below $y = y^*$)

$$\langle \delta y \rangle = y_b - \langle y \rangle, \tag{8}$$

where $y_b = 1.08$ is the rapidity of the projectile in the center-of-mass system, and

$$\langle y \rangle = \int_0^{y_b} y \frac{dn}{dy} dy \Bigg/ \int_0^{y_b} \frac{dn}{dy} dy. \tag{9}$$

This equation refers to net-baryons, i.e. baryons minus antibaryons. At NICA energies, however, the production of antibaryons is so small that the difference between baryons and net-baryons is negligible.

The $\langle \delta y \rangle$ values for 0–40% central and 40–80% central Ar+A collisions are listed in table 5. A clear trend is observed: $\langle \delta y \rangle$ increases with the target mass and with centrality. This behavior is expected because the probability of multiple

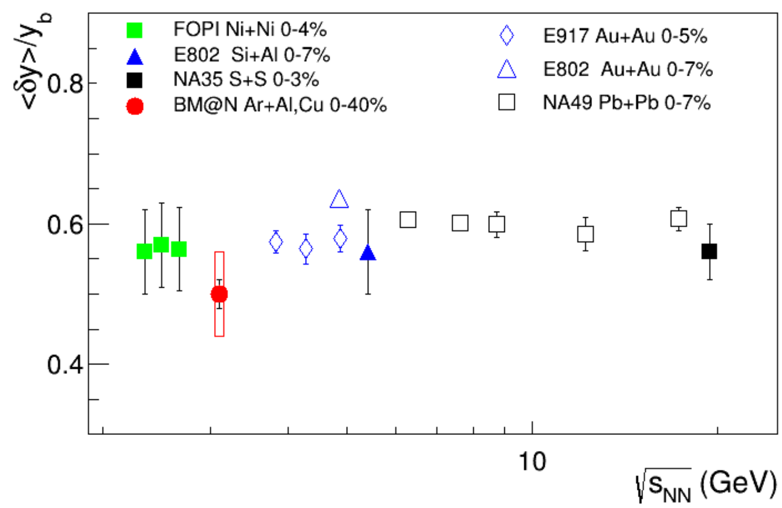

Figure 18. The excitation function of the scaled average rapidity loss $\langle \delta y \rangle / y_b$ in nucleus-nucleus collisions. Medium-size colliding systems [60, 62, 63] are drawn by solid symbols, while heavy systems [60, 64, 65] are shown by open ones. Centrality intervals are indicated in the legends. The BM@N data point is the average of Ar+Al and Ar+Cu results, the systematic error is shown by the box.

interactions in the projectile-target overlap region also rises with centrality and target mass. The quoted uncertainties (statistical errors) are the standard errors of the mean $\langle y \rangle$ calculated from the data points within the rapidity range $[0, y_b]$. The systematic error in the rapidity loss values comes from the uncertainty in the fitting procedure used to describe the baryon rapidity spectra. This uncertainty is taken as the difference between the total baryon number estimated from the fit function and the one obtained from data points. It varies from 7% to 12%.

Figure 18 shows the energy dependence of the scaled average rapidity shift $\langle \delta y \rangle / y_b$ in nucleus-nucleus collisions as a function of $\sqrt{s_{NN}}$. The average of the BM@N results obtained in Ar+Al and Ar+Cu collisions is shown together with results from medium-size almost symmetric colliding systems from [60, 62, 63] (solid symbols) and those from heavy colliding systems [60, 64, 65] (open symbols). The corresponding centrality intervals are indicated in the legends. As one can see, the scaled rapidity loss does not vary significantly over a broad energy range.

10 Particle ratios

The rapidity and centrality dependence of the deuteron-to-proton ratio R_{dp} in Ar+A collisions at 3.2 A GeV ($\sqrt{s_{NN}} = 3.1$ GeV) is presented in figure 19 (a)–(e).Collisions with centrality 0–40% central and 40–80% are represented by solid and open symbols, respectively. As one can see, R_{dp} rises strongly from midrapidity to the beam rapidity in more peripheral collisions. The same trend is observed in 0–40% central Ar+C collisions. In contrast, in 0–40% central collisions of argon nuclei with aluminum or heavier targets, R_{dp} indicates a plateau-like behavior near midrapidity followed by an increase toward the beam rapidity region. The plateau region for R_{dp} increases gradually with the target mass number covering almost all the measured rapidity range in Ar+Pb collisions.

The midrapidity R_{dp} values from 0–40% central and 40–80% central Ar+A collisions as a function of the midrapidity baryon density $\mathrm{d}n_B/\mathrm{d}y$ (obtained from the fits of figure 17) are presented in figure 19 (f). As one can see, R_{dp} increases steadily for small values of $\mathrm{d}n_B/\mathrm{d}y$ and then levels off at higher values.

For a system in chemical equilibrium and a size substantially larger than the deuteron radius, the ratio of the invariant yield of deuterons to the one of protons

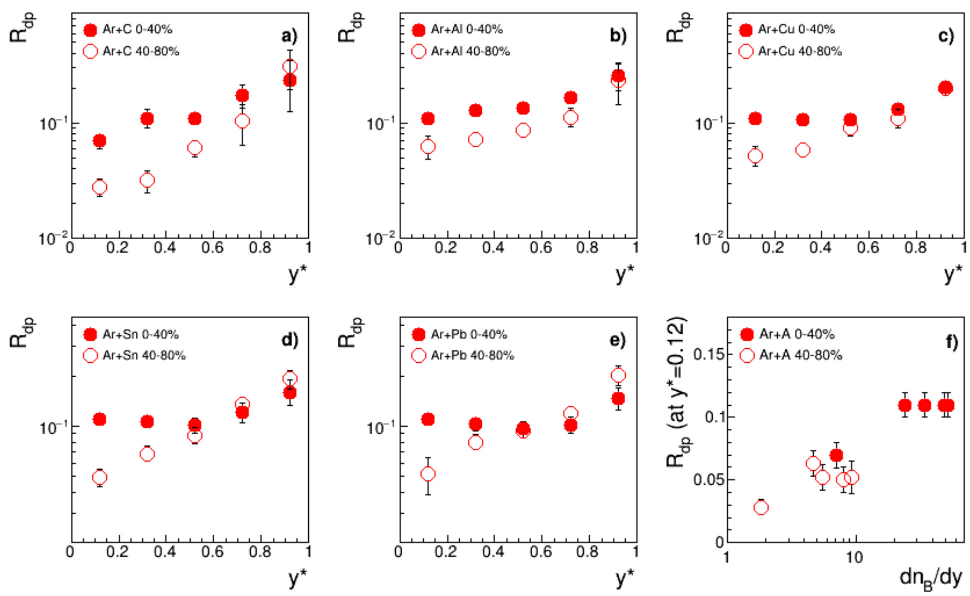

Figure 19. R_{dp} as a function of center-of-mass rapidity y^* in Ar+C (a), Ar+Al (b), Ar+Cu (c), Ar+Sn (d), and Ar+Pb (e) collisions. Results for 0-40% and 40-80% central collisions are shown by solid and open symbols, respectively. Panel (f): Midrapidity R_{dp} as a function of midrapidity baryon density dn_B/dy in Ar+A collisions.

.

can be related to the average proton phase-space density at freeze-out $\langle f_p \rangle$ as

$$\langle f_p \rangle = \frac{R_{pn}}{3} \frac{E_d \frac{d^3 N_d}{d^3 P}}{E_p \frac{d^3 N_p}{d^3 p}}, \tag{10}$$

where R_{pn} is the proton-to-neutron ratio, $P = 2p$, and the factor of 3 accounts for the spins of the particles [13]. The $\langle f_p \rangle$ value depends on the strength of the nuclear stopping in the reaction as well as on the outward flow effects.

Figure 20 (left panel) shows the p_T-dependence of the average proton's phase-space density. Here, the ratio of deuterons to protons is obtained in the rapidity range $0.02 < y^* < 0.42$ and at three p_T/A values: 0.15, 0.3, and 0.45 GeV/c; the $\langle f_p \rangle$ values are calculated according to eq. 10. The values of the R_{pn} ratio in the chosen phase-space region were taken from the UrQMD model. As one can see, $\langle f_p \rangle$ decreases with p_T in all reaction systems. Such a trend is indeed expected for a thermal source at a low phase-space density ($f << 1$), where $\langle f_p \rangle$ follows a Boltzmann distribution and decreases exponentially with p_T [66]. The dashed lines in figure 20 show fits to an exponential function $const \cdot \exp(-p_T/p_{T0})$ for $\langle f_p \rangle$ from Ar+C and Ar+Pb reactions (p_{T0} is the inverse slope parameter). It is known that the presence of outward flow in the system makes $f(p_T)$ flatter as the radial velocity increases [67]. The right panel of figure 20 shows the system size dependence of the slope parameter p_{T0} of the p_T-dependence for $\langle f_p \rangle$. As one can see, this dependence is, indeed, correlated with the results on the radial velocity presented in table 3: i.e., weak radial expansion in Ar+C and approximately the same strength of collective radial flow in Ar+Al, Cu, Sn and Pb.

It was identified long time ago that the nuclear cluster abundances and the entropy value attained in the collisions are related. According to an early investigations [68], in a mixture of nucleons and deuterons in thermal and chemical equilibrium, the entropy per nucleon S_N/A can be deduced from the deuteron-to-proton ratio R_{dp} as

$$\frac{S_N}{A} = 3.945 - \ln R_{dp} - \frac{1.25 R_{dp}}{1 + R_{dp}}. \tag{11}$$

Furthermore, as the collision energy increases, the contribution of mesons S_π to the total entropy becomes important. Following [69], the entropy of pions per nucleon can be estimated by

$$\frac{S_\pi}{A} = 4.1 \frac{N_\pi}{N_N}, \tag{12}$$

where $N_N = N_p + N_n$ is the total number of nucleons.

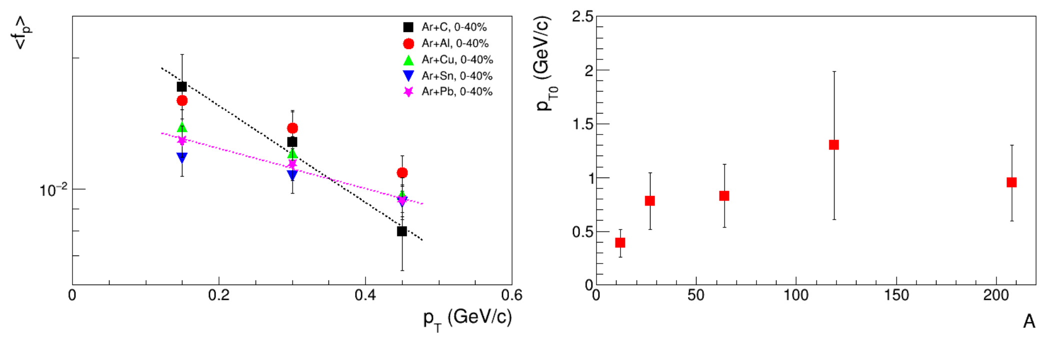

Figure 20. Left: Average proton phase-space density for 0–40% central Ar+A collisions as a function of p_T within the rapidity range 0.02< y^* <0.42. Dashed lines show fits to exponent (see text for details). Right: The inverse slope parameter p_{T0} of the p_T-dependence of $\langle f_p \rangle$ as a function of the target mass number.

We thus calculated the total entropy S/A near midrapidity as the sum of the nucleon and pion entropy contributions according to eqs. 11 and 12. To estimate S_π, we used the recently published BM@N results on positively charged pions [8], while the contribution of π^-, π^0, and neutrons was obtained from the UrQMD model. We found that the contribution of pions to the total entropy does not exceed 25% in Ar+A collisions at NICA energies. Finally, S/A is found to be 10.3, 7.8, 7.8, 7.9, and 7.9 in central Ar+C, Ar+Al, Ar+Cu, Ar+Sn, and Ar+Pb, respectively. The estimated uncertainty in S/A is about 15%. In figure 21 we present the energy dependence of S/A in central heavy-ion collisions. This compilation includes data from experiments that have published numerical values for the midrapidity yields of charged pions, protons, and light nuclei [42, 62, 70–74]. In this figure, we show the BM@N 'saturation' S/A-value of 7.9. As can be seen from the figure, the total entropy increases steadily with collision energy.

It has been established experimentally that the cluster production yields scaled by the spin degeneracy factor (2J+1) decrease exponentially with the atomic mass number A [42, 75]. As an example, figure 22 (left panel) presents dn/dy/(2J+1) at midrapidity for p, d, t as a function of A from 0–40% central Ar+Sn collisions. The particle rapidity density values are extracted from the fits of figure 7. The A-dependence of the yields was fitted to a form:

$$\frac{dn}{dy}(A) = const/p^{A-1}, \tag{13}$$

where the parameter p ('penalty factor') determines the penalty for adding one

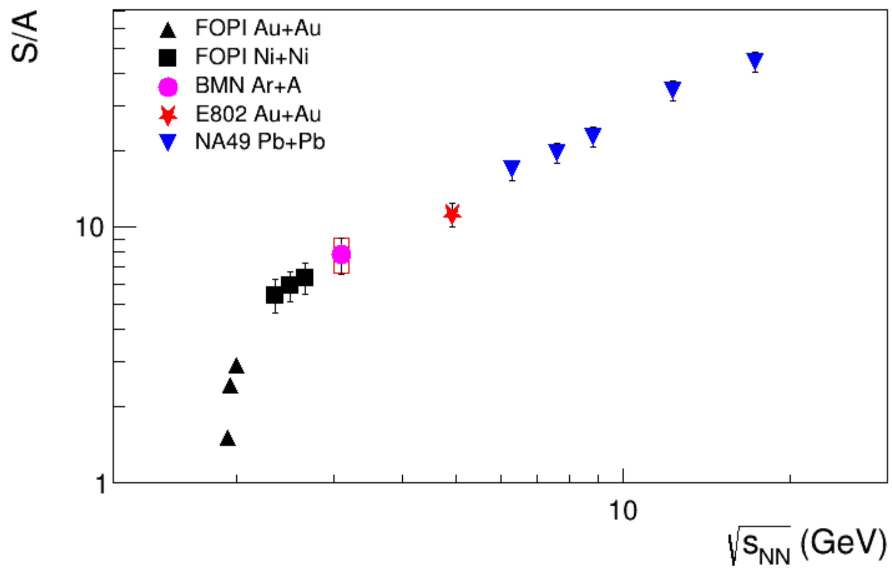

Figure 21. The excitation function of the entropy per baryon S/A from SIS/FOPI [62, 70], AGS/E802 [71], SPS/NA49 [42, 72–74] and NICA/BM@N (this study).

661 extra nucleon to the system.

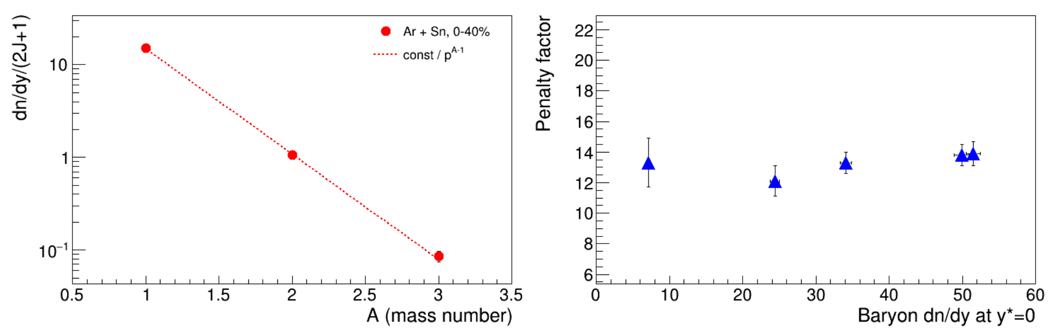

Figure 22. Left: Midrapidity dn/dy/(2J+1) for p, d, t from central Ar+Sn collisions. The dashed line is a fit to eq. 13. Right: Penalty factor from central Ar+A collisions versus baryon rapidity density at midrapidity.

662 The p-factors from central Ar+A collisions are shown in figure 22 (right panel)
663 as a function of the midrapidity baryon rapidity density. The errors are the statis-
664 tical errors obtained from the fit to eq. 13.

Recently, the STAR experiment reported measurements of the compound yield ratio $R_{ptd} = N_p N_t / N_d^2$ of protons (N_p) and tritons (N_t) to deuterons (N_d) [57]. Coalescence models predict [76] that a non-monotonic behavior of the ratio as a function of the system size or collision energy is a signature of the neutron density fluctuations Δn: $R_{ptd} \approx g(1 + \Delta n)$ with a color factor $g \simeq 0.29$. Following this argument, R_{ptd} is a promising observable to search for the critical point and/or a first-order phase transition in heavy-ion collisions [77]. In coalescence models, the compound yield ratio should increase as the size of the system decreases. Indeed, this effect is observed by the STAR experiment [58].

Table 6. $N_p N_t / N_d^2$ values evaluated from the mean dN/dy values of protons, deuterons and tritons over the rapidity range $-0.18 < y^* < 0.22$ and $0.22 < y^* < 0.62$ in Ar+A interactions with centrality 0–40%. The quoted errors are the quadratic sums of the statistical and systematic uncertainties.

	Ar+C	Ar+Al	Ar+Cu	Ar+Sn	Ar+Pb
$N_p N_t / N_d^2$ $(-0.18 < y^* < 0.22)$	0.52 ± 0.18	0.53 ± 0.10	0.66 ± 0.16	0.68 ± 0.12	0.57 ± 0.11
$N_p N_t / N_d^2$ $(0.22 < y^* < 0.62)$	-	0.40 ± 0.07	0.60 ± 0.08	0.50 ± 0.08	0.51 ± 0.12

To evaluate the R_{ptd} ratio, mean values of the dN/dy distributions for protons, deuterons and tritons are calculated in two rapidity ranges: $0.9 < y < 1.3$ $(-0.18 < y^* < 0.22)$ and $1.3 < y < 1.7$ $(0.22 < y^* < 0.62)$. The results are given in table 6 for argon-nucleus interactions with centrality 0–40%. The quoted error is the quadratic sum of the statistical and systematic uncertainties. No significant variation of the $N_p N_t / N_d^2$ values is observed with the various targets. Taking the differences as systematic uncertainties, the weighted average value of the compound ratio is estimated to be 0.59 ± 0.065 for $-0.18 < y^* < 0.22$ and 0.46 ± 0.10 for $0.22 < y^* < 0.62$, where the uncertainty is the quadratic sum of the statistical and systematic uncertainties. Within the uncertainties, there is no strong dependence of the R_{ptd} ratio on rapidity in the measured rapidity range. The BM@N value for R_{ptd} for $-0.18 < y^* < 0.22$ is compared in figure 23 with the measurements of other experiments. The BM@N result lays between the values of 0.8–1.0 derived by the FOPI experiment (impact parameter $b_0 < 0.15$) [43] at lower energies and the values of 0.4–0.5 obtained by the E864 (0–10% central) [53], STAR

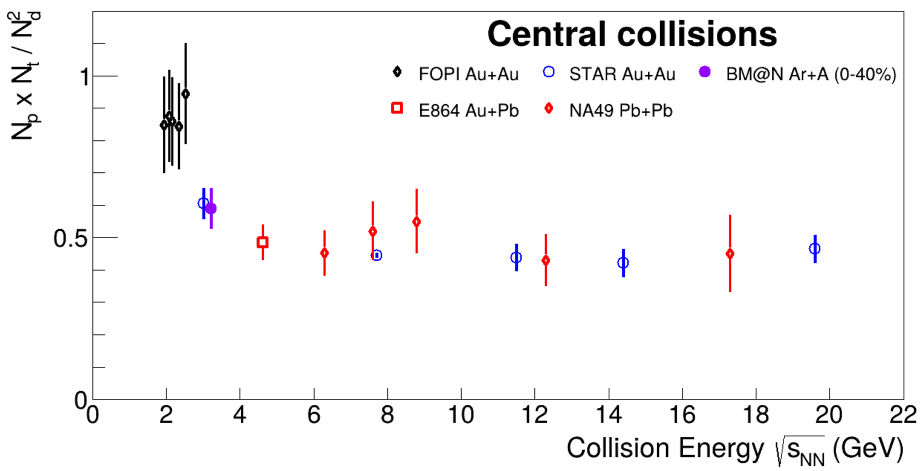

Figure 23. Compound yield ratio $N_p \cdot N_t/N_d^2$ of protons (N_p) and tritons (N_t) to deuterons (N_d^2) as a function of the center-of-mass energy of nucleus-nucleus interactions. The BM@N result represents the weighted average value in the rapidity range $-0.18 < y^* < 0.22$ calculated for Ar+Al, Cu, Sn and Pb interactions with centrality 0–40%.

(0–10% central) [57, 58, 78] and NA49 (0–7% central) [42] experiments at higher CM energies from 4.3 to 18 GeV. The BM@N value for R_{ptd} is consistent with the STAR Au+Au result measured in the fixed target mode at $\sqrt{s_{NN}}$ of 3 GeV [39].

11 Summary

The first results of the BM@N experiment are presented on the proton, deuteron and triton yields and their ratios in argon-nucleus interactions at the beam kinetic energy of 3.2 A GeV. They are compared with the DCM-SMM and PHQMD models and with previously published results of other experiments.

The transverse mass m_T spectra are measured and the mean transverse kinetic energy $\langle E_T \rangle = \langle m_T \rangle - m$ are presented for more central 0–40% events as functions of the rapidity y and mass m of the nuclear fragment. The $\langle E_T \rangle$ values are found to depend linearly on the mass m. The source temperature at kinetic freeze-out and the average radial velocity are extracted.

The rapidity density dN/dy of protons, deuterons and tritons are presented for the whole p_T range in two centrality ranges. The DCM-SMM and PHQMD models reproduce the shapes of the spectra but underestimate the deuteron yields by factors of about 5 and 2, respectively. The triton yields predicted by the models are below the experimental data by a factor of about 5.

The average rapidity loss $\langle \delta y \rangle$ increases with the target mass and with the collision centrality. In contrast, the rapidity loss scaled to the beam rapidity $\langle \delta y \rangle / y_b$ in almost symmetric heavy-ion collisions does not vary significantly over a broad energy range.

The ratio of deuterons to protons R_{dp} rises in peripheral collisions and levels off in central ones, possibly indicating a saturation of the nucleon phase-space density at freeze-out. The entropy per baryon S/A was estimated to be $S/A \approx 8$ nicely fitting in the trend of the S/A energy dependence established from other experimental results.

The freeze-out fireball parameters T obtained from the transverse mass spectra and the baryo-chemical potential μ_B derived from a coalescence analysis were found to follow the trend of the world T, μ_B values obtained from a statistical analysis of particle abundances.

The deuteron to proton and triton to proton yield ratios are used to calculate the coalescence parameters B_2 and B_3 for deuterons and tritons. The coalescence radii of the deuteron and triton source are extracted from the B_2 and B_3 values extrapolated to $p_T = 0$ and compared with results of other experiments.

The compound yield ratio $N_p N_t / N_d^2$ of protons and tritons to deuterons is evaluated and compared with other measurements at lower and higher energies. The results follow the general trend of decreasing values of B_2, B_3 and $N_p N_t / N_d^2$ ratio with increasing energy.

Acknowledgments. The BM@N Collaboration acknowledges the efforts of the staff of the accelerator division of the Laboratory of High Energy Physics at JINR that made this experiment possible. The BM@N Collaboration acknowledges support of the HybriLIT of JINR for the provided computational resources. The research has been supported by the Ministry of Science and Higher Education of the Russian Federation, Project "New Phenomena in Particle Physics and the Early Universe" No. FSWU-2023-0073 and by the Science Committee of the Ministry of Science and Higher Education of the Republic of Kazakhstan (Grant No. AP23487706).

References

[1] B. Friman, W. Nörenberg, and V.D. Toneev, Eur. Phys. J. A 3 (1998).

[2] J. Randrup and J. Cleymans, Phys. Rev. C 74 (2006) 047901.

[3] Ch. Fuchs, Prog. Part. Nucl. Phys. 56 (2006) 1-103.

[4] NICA White Paper, Eur. Phys. J. A 52 (2016).

[5] BM@N Conceptual Design Report: http://nica.jinr.ru/files/BM@N/BMN_CDR.pdf.

[6] M. Kapishin (for the BM@N Collaboration), Nucl. Phys. A 982 (2019) 967-970.

[7] M. Kapishin (for the BM@N Collaboration), SQM 2019 proceedings, 285 Springer Proc. Phys. 250 (2020) 21-27.

[8] S.Afanasiev et al. (BM@N Collaboration), JHEP 07 (2023) 174.

[9] W. Busza and A. S. Goldhaber, Phys. Lett. 139B, 235 (1984).

[10] G.C. Rossi and G. Veneziano, Phys. Rep. 63 (1980) 153.

[11] A. Capella and B. Z. Kopeliovich, Phys. Lett. B 381, 325 (1996).

[12] D. Kharzeev, Phys. Lett. B 378, 238 (1996).

[13] M.Murray and B. Holzer, Phys Rev. C 63, 054901 (2000).

[14] A. Andronic, P. Braun-Munzinger, and J. Stachel, Phys. Lett. B 673, 142 (2009).

[15] T.A. Armstrong et al (E864 Collaboration) Phys. Rev. Lett. 83, 5431 (1999).

[16] G. Bertsch and J. Cugnon, Phys. Rev. C 24, 2514 (1981).

[17] J. I. Kapusta, Phys. Rev. C 24, 2545 (1981).

[18] S.T. Butler and C.A. Pearson, Phys. Rev. 129, 836 (1963).

[19] A. Schwarzschild and C. Zupancic, Phys. Rev. 129, 854 (1963).

[20] S. Mrowczynski, Phys. Lett. B 277, 43 (1992).

[21] H. Sato, K. Yazaki, Phys. Lett. 98B (1981) 153.

[22] R. Scheibl and U. Heinz, Phys. Rev. C 59, 1585 (1999).

[23] N. Amelin, K. Gudima, and V. Toneev, Sov. J. Nucl. Phys. 51, 1093 (1990).

[24] M. Baznat, A. Botvina, G. Musulmanbekov, V. Toneev, V. Zhezher, Phys. Part. Nucl. Lett. 17 (2020) no. 3; arXiv: 1912.09277v2.

[25] J.Aichelin, E. Bratkovskaya et al, Phys. Rev. C 101, 044905 (2020).

[26] BM@N project:
https://bmn.jinr.int/detector/project/BMN_project.pdf.

[27] S. Afanasiev et al., Nucl. Instrum. Meth. A 1065 (2024) 169532.

[28] D. Baranov et al., JINST 12 (2017) no. 06, C06041.

[29] V. Babkin et al., Nucl. Instrum. Meth. A 824, P.490-492 (2016); V. Babkin et al., Proceedings of Science, 2014, Vol.213 (Proceedings of TIPP-2014), P.289.

[30] N. Kuzmin et al., Nucl. Instrum. Meth. A 916, P. 190-194 (2019).

[31] K. Alishina et al., Phys. Part. Nucl., 53 (2022) no. 2, 470-475.

[32] V. Akishina and I. Kisel, J. Phys.: Conf. Ser. 599, 012024 (2015), I. Kisel, Nucl. Instrum. Meth. A 566, 85 (2006).

[33] CERN Program Library, Long Writeup W5013, Geneva, CERN, 1993.

[34] https://git.jinr.ru/nica/bmnroot.

[35] V.Plotnikov, L.Kovachev, A.Zinchenko, Phys. Part. Nuclei Lett. 20 (2023), 1392–1402.

[36] K.Kanaki, PhD Thesis, Technische Universität Dresden, 2007.

[37] H.Angelov et al., P1-80-473, JINR, Dubna.

[38] BM@N web-page:
https://bmn.jinr.int/wp-content/uploads/2025/02/
Tabulated-results-from-the-paper.pdf.

[39] M.I.Abdulhamid et al. (STAR Collaboration) Phys. Rev. C 110, 054911 (2024).

[40] V.Vovchenko et al, Phys. Lett. B 809 (2020) 135746.

[41] D.R.Tilley, H.R. Weller, G.M. Hale, Nucl. Phys. A 541 (1992) 1.

[42] T.Anticic et al. (NA49 Collaboration) Phys. Rev. C 94, 044906 (2016).

[43] W.Reisdorf et al. (FOPI Collaboration) Nucl.Phys.A 848 (2010) 366-427.

[44] M.A.Lisa et al. (EOS Collaboration) Phys.Rev.Lett.75 (1995) 2662.

[45] L.Kumar (for the STAR Collaboration), Nucl. Phys. A 931, 1114 (2014).

[46] L.Adamczyk et al. (STAR Collaboration) Phys.Rev.C 96 (2017) 4, 044904.

[47] Hui Liu for the STAR Collaboration, Acta Physica Polonica B Proceedings Supplement 16, 1-A148 (2023).

[48] E.Schnedermann, J.Sollfrank, and U.W.Heinz, Phys.Rev.C 48 (1993) 2462.

[49] A.Z.Mekjian, Phys. Rev. Lett. 38, 640 (1977); Phys. Rev. C 17, 1051 (1978); and Nucl. Phys. A 312, 491 (1978).

[50] J.I.Kapusta, Phys. Rev. C 21, 1301 (1980).

[51] PDG group review, J. Phys. G 37, 075021 (2010), Introduction, section 5.2.

[52] I.G.Bearden et al. (NA44 Collaboration), Eur. Phys. J. C 23, 237–247 (2002).

[53] T.A.Armstrong et al. (E864 Collaboration), Phys. Rev. C 61, 064908 (2000), nucl-ex/0003009.

[54] J.Barrette et al. (E877 Collaboration), Phys. Rev. C61,044906 (2000).

[55] M.J.Bennett et al. (E878 Collaboration), Phys. Rev. C58, 1155 (1998).

[56] G.Ambrosini et al. (NA52 Collaboration), Phys. Lett. B 417, 202 (1998).

[57] M.I.Abdulhamid et al. (STAR Collaboration), Phys.Rev.Lett. 130 (2023) 202301.

[58] D.Zhang (for the STAR Collaboration), Nucl. Phys. A 1005, 121825 (2021).

[59] I.G.Bearden et al. (BRAHMS Collaboration), Phys. Rev. Lett. 93, 102301, 2004.

[60] F.Videbaek and Ole Hansen, Phys. Rev. C 52 (1995) 2684.

[61] S.A.Bass et al., Prog. Part. Nucl. Phys. 41 225 (1998).

[62] B.Hong et al (FOPI Collaboration), Phys. Rev. C 57 (1998) 244.

[63] J.Bachler et al (NA35 Collaboration), Phys. rev. Lett. 72 (1994) 1419.

[64] B.B.Back et al (E917 Collaboration), Phys. Rev. Lett. 86 (2001) 1970.

[65] C.Blume, for the NA49 Collaboration, J. Phys. G 34 (2007) S951.

[66] M.J.Murray, J. Phys. G 28, 2069 (2002).

[67] B.Tomasik and U.Heinz, Phys. Rev. C 65, 031902(R) (2002).

[68] L.P.Csernai and J. I. Kapusta, Phys. Rep. 131, 4 (1986) 223–318.

[69] S. Z.Belenkij and L.D.Landau, Nuovo Cimento, Supplement 3, 15 (1956).

[70] G.Poggi et al (FOPI Collaboration), Nucl. Phys. A 586, 755 (1995).

[71] L.Ahle et al (E802 Collaboration) Phys. Rev. C 60, 064901 (1999).

[72] T.Anticic et al (NA49 Collaboration), Phys. Rev. C 69, 024902 (2004).

[73] C.Alt et al (NA49 Collaboration), Phys. Rev. C 77, 024903 (2008).

[74] T.Anticic et al. (NA49 Collaboration), Phys.Rev.C 85 (2012) 044913.

[75] T.A.Armstrong et al (E864 Collaboration), Phys. Rev. C 61,064908 (2000).

[76] K.-J.Sun et al., Phys.Lett.B 774 (2017) 103.

[77] D.Oliinychenko, Nucl.Phys.A 1005 (2021) 121754.

[78] M.I.Abdulhamid et al. (STAR Collaboration), Phys.Rev.Lett. 130 (2023) 202301.